

# Gas flow in barred potentials - III. Effects of varying the Quadrupole.

Mattia C. Sormani, James Binney and John Magorrian

<sup>1</sup> *Rudolf Peierls Centre for Theoretical Physics, 1 Keble Road, Oxford OX1 3NP*

## ABSTRACT

We run hydrodynamical simulations of a 2D isothermal non self-gravitating inviscid gas flowing in a rigidly rotating externally imposed potential formed by only two components: a monopole and a quadrupole. We explore systematically the effects of varying the quadrupole while keeping fixed the monopole and discuss the consequences for the interpretation of longitude-velocity diagrams in the Milky Way. We find that the gas flow can constrain the quadrupole of the potential and the characteristics of the bar that generates it. The exponential scale length of the bar must be at least 1.5 kpc. The strength of the bar is also constrained. Our global interpretation favours a pattern speed of  $\Omega = 40 \text{ km s}^{-1} \text{ kpc}^{-1}$ . We find that for most observational features, there exist a value of the parameters that matches each individual feature well, but is difficult to reproduce all the important features at once. Due to the intractably high number of parameters involved in the general problem, quantitative fitting methods that can run automatic searches in parameter space are necessary.

**Key words:** ISM: kinematics and dynamics – galaxies: kinematics and dynamics

## 1 INTRODUCTION

It is now well-established that the Milky Way is a barred galaxy (e.g. Stanek et al. 1994; Dwek et al. 1995; Binney et al. 1997; Wegg & Gerhard 2013, see also Fux 2004; Gerhard & Wegg 2014 for reviews). Many authors have modelled the gas flow in the Milky way and compared it with the available data (Mulder & Liem 1986; Binney et al. 1991; Jenkins & Binney 1994; Weiner & Sellwood 1999; Englmaier & Gerhard 1999; Lee et al. 1999; Fux 1999; Bissantz et al. 2003; Rodriguez-Fernandez & Combes 2008; Baba et al. 2010; Pettitt et al. 2014, 2015). However, a number of issues remain unresolved and the data still contain a wealth of information capable of constraining the Galactic potential that has yet to be fully exploited by gas dynamical models (Sormani & Magorrian 2015).

In two previous papers (Sormani et al. 2015a,b, hereafter SBM15a and SBM15b) we investigated the dynamics of gas flow in barred potentials. We studied in detail the relation between the flow of a 2D isothermal non self-gravitating inviscid gas and closed ballistic orbits in the same externally imposed rigidly rotating barred potential. We found that hydro streamlines closely follow ballistic closed orbits at large and small radii, and tiny deviations of the hydro streamlines from ballistic closed orbits generate bar-driven spiral arms as kinematic density waves. At intermediate radii shocks arise and the streamlines shift between two families of closed orbits. We showed that the sound speed in the gas and the spatial resolution of the grid both affect the gas flow significantly.

In SBM15a we discussed the implications of our simulations for the interpretation of longitude-velocity diagrams (hereafter  $(l, v)$  diagrams) of atomic (HI) and molecular (CO, CS) gas in the Milky Way. The simulations presented in SBM15a were based

on the Binney et al. (1991) barred potential, which was originally used to construct a picture of the flow of gas through the central few kiloparsecs of our Galaxy on the assumption that gas follows closed orbits. Our simulations provided strong support for this assumption, but refined the Binney et al. (1991) picture of gas flow in several respects. Specifically: (i) In Binney et al. (1991) the parallelogram in the  $(l, v)$  plot for CO was interpreted as the trace of the cusped orbit, while we found that the shocks form two sides of the CO parallelogram, and conjectured that the prominence of the CO parallelogram is due to efficient conversion of atomic gas into molecular gas. (ii) Binney et al. (1991) did not have an explanation for the observed asymmetry in the distribution of molecular emission near the Galactic centre, while we argued that a promising explanation for the asymmetry is provided by the way the *wiggle instability* (Wada & Koda 2004; Kim et al. 2014) makes the flow through the shocks unstable. The large fluctuations generated by this instability might cause the conversion efficiency to fluctuate wildly and give rise to gross asymmetry in the distribution of molecular gas.

However, since we did not keep track of the chemistry of the ISM, items (i) and (ii) remained merely promising conjectures.

SBM15a identified two key features of the observed  $(l, v)$  diagrams that were still unexplained after their revision of the Binney et al. (1991) model: (i) Coherent broad features like the 3 kpc arm and its counterpart on the far side of the Galaxy (Dame & Thaddeus 2008) – these were absent from the simulations of SBM15a. (ii) Forbidden emission at large longitudes – in the SBM15a models forbidden emission covers a significantly smaller portion of the  $(l, v)$  diagram than in the data.

arXiv:1507.03078v3 [astro-ph.GA] 2 Nov 2017

SBM15a suggested two main directions for improving their models: First, inclusion of a law for the conversion of gas between atomic and molecular forms, so when gas is compressed at a shock much of it is converted to molecular gas. Second, modification of the quadrupole moment of the bar, since a higher quadrupole moment should generate stronger spiral arms and stronger non-circular motions, which are the likely explanations for internal features and forbidden velocity emission in the observational  $(l, v)$  diagrams. SBM15b explored the mechanism by which the bar generates the spirals that are responsible for internal structure in the  $(l, v)$  plane. Consequently, we here implement the second upgrade recommended by SBM15a by systematically exploring the effects on the gas flow of a variation of the quadrupole component of the potential, and discuss the consequence of this variation for the interpretation of Milky Way  $(l, v)$  diagrams.

In Section 2 we explain our numerical methods. In Section 3 we enumerate the bar's signatures in the  $(l, v)$  plane. In Section 4 we describe a reference model, which we use to relate structures in the galactic plane to those in the  $(l, v)$  plot. In Section 5 we study how the structure of the  $(l, v)$  plane changes as we change the parameters defining the bar. In Section 6 we outline the extent to which the Galactic bar is constrained by the observed  $(l, v)$  diagrams, and in Section 7 we sum up and consider promising directions for future work.

## 2 METHODS

### 2.1 The potential

We assume that the gas flows in a simple externally imposed two-dimensional barred potential that rotates at constant pattern speed  $\Omega_p$ . The potential can be expanded in multipoles

$$\Phi(R, \phi) = \Phi_0(R) + \sum_{m=1}^{\infty} \Phi_m(R) \cos(m\phi + \phi_m), \quad (1)$$

where  $\{R, \phi\}$  are planar polar coordinates,  $\phi_m$  are constants and  $\Phi_m$  are functions of  $R$  only. We assume that the potential comprises only monopole and quadrupole terms, so

$$\Phi(R, \phi) = \Phi_0(R) + \Phi_2(R) \cos(2\phi). \quad (2)$$

The solid line in Fig. 1 shows the circular speed  $v_c$  implied by the monopole  $\Phi_0(r)$  we adopt in the present paper, while the dashed line shows  $v_c$  for the monopole used by Jenkins & Binney (1994) and SBM15a. The latter monopole is unrealistic at large  $R$  because its circular speed becomes excessive, whereas the monopole used here coincides with the monopole of Sormani et al. (2015a) at small radii but at greater radii generates a circular speed that plateaus at  $220 \text{ km s}^{-1}$ . The dot-dashed line shows for comparison the circular speed of the Binney et al. (1991) potential. The potential used in Jenkins & Binney (1994) and SBM2015a differs from the potential used in Binney et al. (1991) only by the addition of an axisymmetric disc component.

Our quadrupole  $\Phi_2$  is generated by the density distribution

$$\rho_2(r, \phi, \theta) = \frac{KA}{r_q^2} \exp\left(-\frac{2r}{r_q}\right) \sin^2 \theta \cos(2\phi), \quad (3)$$

where  $\{r, \theta, \phi\}$  are spherical coordinates with the  $\theta = 0$  axis point-

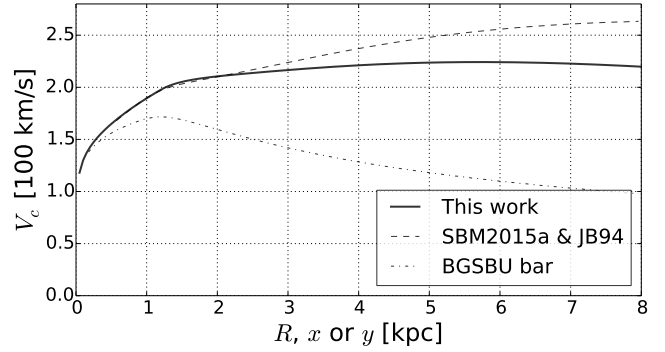


**Figure 1.** Circular speeds. Solid Line: potential used in this paper. Dashed line: potential used in Jenkins & Binney (1994); Sormani et al. (2015a). Dot-dashed line: potential used in Binney et al. (1991). All the curves in this picture are calculated from the monopole component of each potential.

ing towards the north galactic pole. The constants are<sup>1</sup>

$$K = \frac{v_0^2}{4\pi G} \exp(2), \quad (4)$$

with  $v_0 = 220 \text{ km s}^{-1}$  and  $G$  is the gravitational constant. The two main free parameters of  $\rho_2$  are the quadrupole strength  $A$  and the quadrupole length  $r_q$ . We have chosen the form of the quadrupole density distribution to be exponential as recent infrared photometry has found that the Milky Way bar density profile is roughly exponential (Wegg & Gerhard 2013).

Since  $\rho_2$  is proportional to the real part of  $Y_2^2$ , which is an eigenfunction of the Laplacian operator, the density distribution (3) gives rise to the potential

$$\Phi_2(r, \phi, \theta) = \Phi_2(R) \sin^2 \theta \cos(2\phi). \quad (5)$$

Our simulations are two-dimensional, so we only evaluate  $\Phi_2$  in the plane  $\theta = \pi/2$ . Thus, while the 3D density distribution given by Eq. (3) should not be considered a realistic density distribution for our Galaxy, the resulting 2D potential in the plane can be obtained by a more realistic 3D density distribution. To be physical, a potential must come from a non-negative density distribution. We have checked that when our monopole is realised through a spherical symmetric distribution, the total density distribution is positive for all the values of the parameters used in this paper.

### 2.2 Hydro Simulation Scheme

In our simulations, we assume that the gas is a two-dimensional inviscid isothermal fluid governed by the Euler equations. An additional term is introduced in the continuity equation to implement the recycling law of Athanassoula (1992). The dynamical equations in an inertial frame are

$$\begin{aligned} \partial_t \rho + \nabla \cdot (\rho \mathbf{v}) &= \alpha(\rho_0^2 - \rho^2), \\ \partial_t \mathbf{v} + (\mathbf{v} \cdot \nabla) \mathbf{v} &= -\frac{\nabla P}{\rho} - \nabla \Phi, \\ P &= c_s^2 \rho, \end{aligned} \quad (6)$$

where  $\rho$  is the surface density of the gas,  $P$  is the pressure,  $\Phi$  is the gravitational potential,  $\mathbf{v}$  is the velocity,  $c_s$  is the sound speed,  $\alpha$  is

<sup>1</sup> Note added after publication: this factor has been corrected. The published version contains a typo.

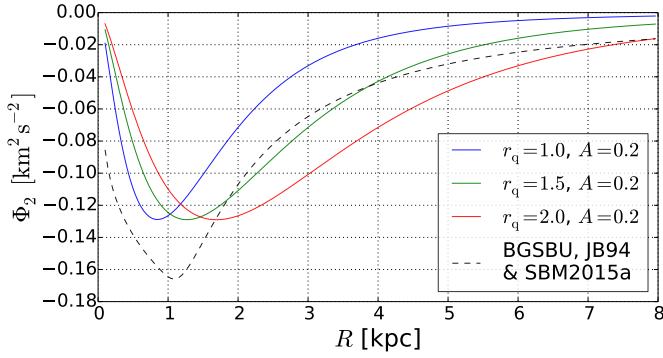


**Figure 2.** The quadrupole component  $\Phi_2$ . In full lines, for the class of potentials used in this paper for the three different values of the bar length  $r_q$  and for a bar strength  $A = 0.2$ . The curves for different values  $A$  are not shown but can be easily obtained by scaling linearly the curves shown. In dashed line the quadrupole component of the bar used in Binney et al. (1991); Jenkins & Binney (1994); Sormani et al. (2015a) is shown for comparison. *Note added after publication:* the y label in this plot should be in units of  $[100\text{km/s}]^2$ , not  $[\text{km/s}]^2$ .

a constant representing the efficiency of the recycling law and  $\rho_0$  is the initial surface density. In our simulations the gas is assumed to be isothermal, hence the sound speed is a constant number which is assumed to be  $c_s = 10\text{km s}^{-1}$ .

The recycling law was originally meant to take into account in a simple way the effects of star formation and stellar mass loss. In practice, the only effect of the recycling law is to prevent too much gas from accumulating in the very centre and to replace gas lost at the boundary due to the outflow boundary conditions. It does not affect the morphology of the results, so our results do not change if we disable the recycling law. We adopt recycling efficiency  $\alpha = 0.3M_\odot\text{pc}^{-2}\text{Gyr}^{-1}$  and initial density  $\rho_0 = 1M_\odot\text{pc}^{-2}$ .

We use a grid-based, Eulerian code based on the second-order flux-splitting scheme developed by van Albada et al. (1982) and later used by Athanassoula (1992), Weiner & Sellwood (1999) and others to study gas dynamics in bar potentials. The implementation used here is the same as was used by SBM15a,b.

We used a grid  $N \times N$  to simulate a square 20kpc on a side, where  $N$  defines the resolution of the simulation. We start with gas in equilibrium on circular orbits in an axisymmetrized potential and, to avoid transients, turn on the non-axisymmetric part of the potential gradually during the first 615Myr. We use outflow boundary conditions: gas can freely escape the simulated region, after which it is lost forever. The potential well is sufficiently deep, however, to prevent excessive quantities of material from escaping.

### 2.3 Projecting to the $(l, v)$ plane

We adopt a very simple projection procedure to produce the predicted  $(l, v)$  distributions for each simulation snapshot  $(\rho(\mathbf{x}), \mathbf{v}(\mathbf{x}))$ . We assume that the Sun is undergoing circular motion at a radius  $R_0 = 8\text{kpc}$  with speed  $\Theta_0 = 220\text{km s}^{-1}$ . Calling  $\phi$  the angle between the major axis and the Sun–GC line, the Cartesian coordinates of the Sun are given by  $x_\odot = R_0 \cos \phi$ ,  $y_\odot = R_0 \sin \phi$ . In our models, we only project material inside the solar circle.

The resolution of our  $(l, v)$  diagrams is  $\Delta l = 0.25^\circ$  in longitude and  $\Delta v = 2.5\text{km s}^{-1}$  in velocity. Along each line of sight, we sample the density and the velocity by linearly interpolating the results of the simulations at points separated by  $\delta s = 1\text{pc}$ . These density measures are accumulated in velocity bins of width

$\Delta v = 2.5\text{km s}^{-1}$ . The final  $(l, v)$  intensity at the chosen longitude in each range of velocity are obtained by summing over all the relevant points along the line of sight weighted by their masses.

This procedure yields a brightness temperature that is linear in column density which is equivalent to the simplest radiative transfer calculation (e.g., Binney & Merrifield 1998, Formula (8.17) and (8.20)). In the case of HI, the brightness temperature is linear in the column density if the gas has constant spin temperature and its optical depth is negligible. So our projection is equivalent to simple HI radiative transfer in the constant-temperature, optically-thin case. The assumption of constant temperature is known to be a simplification for Galactic HI, which is instead often modelled as a medium made by two or more phases at different temperatures (see for example Ferrière 2001). In the case of  $^{12}\text{CO}$ , the brightness temperature is not linearly related to density when considering a single cloud because molecular clouds are typically optically thick at 2.6mm. However, a linear relationship will hold between brightness temperature and the number density of unresolved CO clouds provided the cloud density is low enough for shadowing of clouds to be unimportant (see, e.g., Binney & Merrifield 1998, §8.1.4).

### 3 SIGNATURES OF THE BAR

In the upper panel of Fig. 3 the grey scale shows the intensity in the  $(l, v)$  plane of 2.6mm  $J = 1 \rightarrow 0$  line radiation by CO at  $|l| < 30^\circ$ . Coloured lines schematically trace features identifiable in the CO and 21-cm HI  $(l, v)$  diagrams. The lower panel shows the very different distribution of emission we would expect in the absence of the quadrupole  $\Phi_2$ . The latter has a big impact on  $(l, v)$  diagrams and we explore how the features marked in the upper panel can be used to constrain  $\Phi_2$ . We will in the process indicate where in the Galaxy the gas lies that gives rise to most of these features. The background to our discussion can be found in Burton et al. (1992) and Binney & Merrifield (1998). Fig. 4 shows the longitude-velocity diagrams for 21cm HI data (Kalberla et al. 2005) in the upper panel and of  $^{12}\text{CO}$  data (Dame et al. 2001) in the lower panel.

The key features of the observed  $(l, v)$  plots are

(i) *Emission at forbidden velocities.* If gas everywhere moved on circles, emission in the quadrants  $(l > 0, v < 0)$  and  $(l < 0, v > 0)$  could not be produced by material inside the Sun. Material that lies outside the Sun can produce emission in these quadrants, but at  $|l| < 30^\circ$ , such emission is confined to small values of  $|v|$ . Velocities in the quadrants  $(l > 0, v < 0)$  and  $(l < 0, v > 0)$  that cannot be reached by gas outside the Sun are said to be “forbidden”.

For example, practically all the emission at  $|l| < 5^\circ$ ,  $v > 100\text{km s}^{-1}$  in Fig. 4 comes from inside the Solar circle (but the forbidden emission extends also up to  $|l| \simeq 8^\circ$ ). Forbidden emission is automatically generated by  $\Phi_2$  (e.g. Burton et al. 1992; Binney & Merrifield 1998).

(ii) *Velocity peaks.* At  $|l| \sim 2^\circ$  in Fig. 4 emission is seen at very high velocities,  $|v| \simeq 270\text{km s}^{-1}$ . At one time these peaks were considered evidence of a very centrally concentrated monopole component of the Galactic potential, but since Binney et al. (1991) it has been widely accepted that they are generated by  $\Phi_2$ .

(iii) *Internal features.* The lower panel of Fig. 4 shows a complex pattern of ridges of enhanced emission. Fig. 3 gives the conventional names of the more important structures – more comprehensive lists of features can be found in, for example, Rougoor (1964); van der Kruit (1970); Cohen (1975); Bania (1977); Bally et al. (1988); Dame et al. (2001); Dame & Thaddeus (2008). These

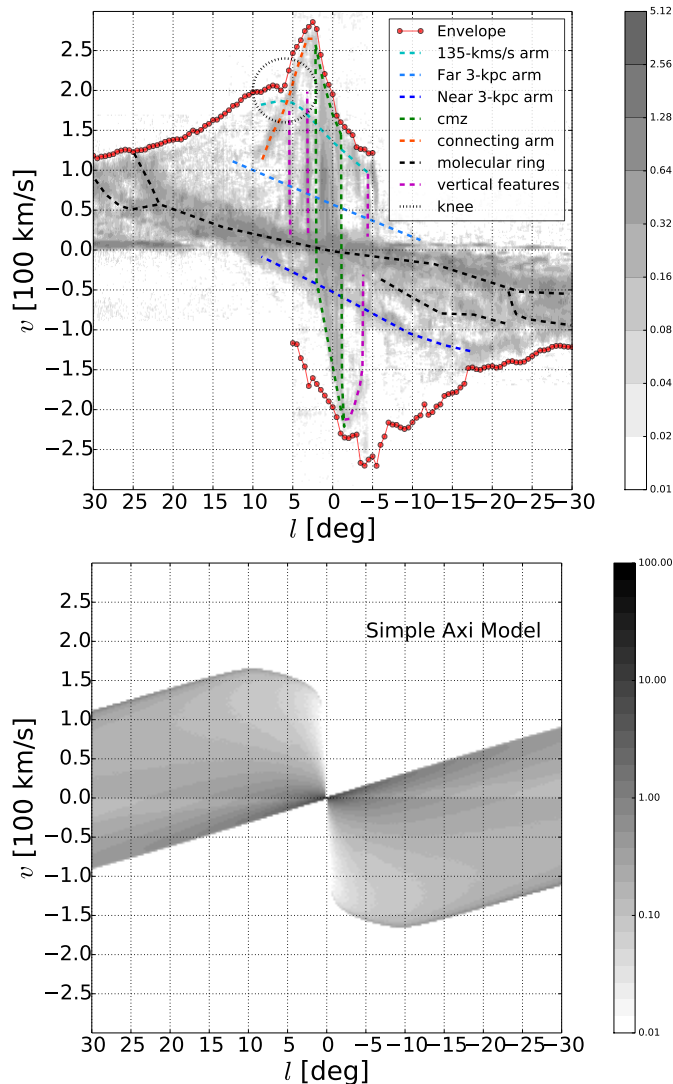


**Figure 3.** Upper panel: CO observations with features superimposed. The red dots trace the envelope determined from HI data as explained in Sormani & Magorrian (2015). Dashed lines trace internal features. The colorbar is in K. Lower panel: appearance of the diagram in the absence of the quadrupole potential under the assumption that the gas density is proportional to  $\exp(-R/2R_0)$ . The colorbar is in arbitrary units.

features would be absent if the gas distribution were axisymmetric (lower panel of Fig. 3).

(iv) *The Envelope.* The red dots in Fig. 3 trace the envelope of the observed emission, determined as explained in Sormani & Magorrian (2015). The envelope carries the imprint of  $\Phi_2$  in three ways: through the velocity peaks, the emission at forbidden velocities, and the shoulders and bumps that arise where an internal feature touches the envelope.

(v) *Bumps on the Envelope.* A mechanism by which spiral arms generate bumps on the envelope is described in §9.1.2 of Binney & Merrifield (1998). We identify as particularly interesting the *knee* marked with a circle in Fig. 3. This knee occurs where the envelope shifts from touching the arm at  $135\text{-km/s}$  to touching the *connecting arm* (green dashed and light red dashed curves in Fig. 3).

(vi) *Tilt.* The central few kiloparsecs of the gas disc appear to be tilted with respect to the Galactic plane such that the far end of the bar lies above, and the near end below, the plane (Liszt & Burton

1980; Burton et al. 1992). It is worth noting in the connection that the structure of the knee changes as we shift in  $b$ . In Figs. 4 and 3 the data are integrated over a range in latitude  $b$ , but if we study slices at different latitudes (Figs. A1 and A2 in Appendix A) we see that the connecting arm, which contributes to the envelope on the low- $l$  side of the knee, appears only at  $b < 0$ , while the arm at  $135\text{ km s}^{-1}$ , which forms the envelope on the other side, appears only at  $b \geq 0$ . This relative offset in  $b$  suggests that the gas disc is moving to larger  $b$  as one moves outwards along the black dotted line in the top right panel of Fig. 5. Since the connecting arm and the arm at  $135\text{ km s}^{-1}$  appear at distinct latitudes, they should represent distinct dynamical features. Thus the knee, which arises from the transition between these structures, cannot reflect merely a sudden change in the circular speed.

(vii) *Clumpiness.* In addition to the coherent features discussed in item (iii), the observed  $(l, v)$  plots show scattered clumpiness on a variety of scales. This clumpiness is believed to reflect clumpiness in real space, and was modeled by Baba et al. (2010) as caused by heating and cooling processes. In general, models that do not include such effects are, in the absence of the wiggle instability, smooth on fine scales. Besides including heating and cooling effects, proper radiative transfer modelling is probably needed to explain the clumpiness in detail.

(viii) *Asymmetry.* Approximately three-quarters of the molecular emission from  $|l| \lesssim 4^\circ$  comes from positive longitudes (e.g. Burton et al. 1992). The cause of this asymmetry is a long-standing puzzle. The asymmetry is too big to be attributed solely to a perspective effect from an inclined bar (Jenkins & Binney 1994). The only promising explanation currently available is that the asymmetry is generated by fluctuations in an unsteady flow (SBM2015a). However, as mentioned in the introduction, this idea remains embryonic and requires further investigation.

(ix) *Variation by species.* Different chemical species HI, CO, CS, etc., are distributed differently throughout the Galaxy because they probe different temperature and density environments. Consequently, each produces a different  $(l, v)$  diagram. A complete model would explain the variation in  $(l, v)$  plots. A related problem is the extent to which gas and dust are correlated (see for example Sale & Magorrian 2014).

Towards the end of the paper we will return to this list to review how items constrain the Galactic bar.

## 4 A REFERENCE MODEL

In this Section, we describe in detail a “reference” model. Table 1 gives the values of its defining parameters. The adopted values of the sound speed ( $c_s = 10\text{ km s}^{-1}$ ) and the angle of the bar to the Sun-GC line ( $\phi = 20^\circ$ ) are the same as those used by SBM15a to facilitate comparison with earlier work. We do, however, adopt a smaller pattern speed ( $\Omega_p = 40\text{ km s}^{-1}\text{ kpc}^{-1}$ ) than that ( $63\text{ km s}^{-1}\text{ kpc}^{-1}$ ) used by Binney et al. (1991) and SBM15a for reasons that will emerge later. The reference model has not been chosen because its parameters give the best fit to the observations; rather, it is just a representative model that displays many of the characteristic of interest for this paper. In later sections, we will see how these characteristics change as a function of the model’s parameters.

The top left panel of Fig. 5 shows the gas density reached after a long time. The bottom left panel of Fig. 5 shows the associated  $(l, v)$  plot for bar angle  $\phi = 20^\circ$ . The top right panel marks with



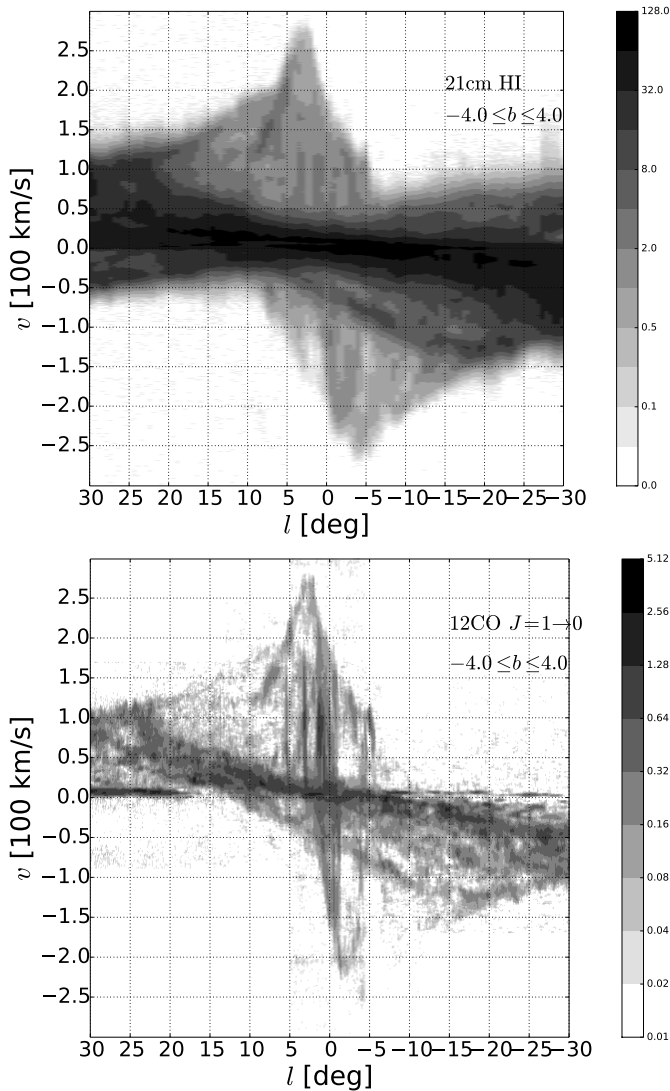


**Figure 4.** Upper panel: HI observations integrated over  $|b| < 4^\circ$ . Lower panel: CO observations integrated over  $|b| < 4^\circ$ . Colorbars units are in K.

coloured lines prominent features in the top left panel. The lower-right panel shows the location of these same features in the  $(l, v)$  plane.

The general characteristics of the gas flow can be understood as described in SBM15a,b and we now briefly summarise their picture. In the outer regions, where spiral arms are present, the velocity field of the gas is well approximated by elongated, closed ballistic  $x_1$  orbits. However, the agreement is not perfect because the streamlines execute small librations around underlying  $x_1$  orbits. These librations generate spiral arms as kinematic density waves (SBM15b). While flowing approximately on  $x_1$  orbits, the gas also slowly drifts inwards. At a transition point, the gas stops following  $x_1$  orbits and two straight offset shocks form. After passing the shocks, the gas plunges towards the central  $x_2$  disc, where it settles and flows to a very good approximation on  $x_2$  orbits. The  $x_2$  disc is shown as the central grey structure in the top right panel of Fig. 5, and the two straight shocks are the red and blue features that just touch the grey structure.

In contrast to the  $(l, v)$  plot generated by circular motion (lower panel of Fig. 3), the  $(l, v)$  plot of the reference model (bot-

tom left panel of Fig. 5) bears a strong resemblance to the observed  $(l, v)$  plots. Because we are interested in the region inside the solar circle, we ignore emission in the quadrants  $(l > 0, v < 0)$ ,  $(l < 0, v > 0)$  other than emission at small  $|l|$  and forbidden velocities. The position and strength of the velocity peaks of the reference model ( $|l| \simeq 3^\circ$ ,  $v \simeq 280 \text{ km s}^{-1}$ ) match well the peaks seen in the observational plots. The region covered by forbidden velocities in the reference model matches reasonably well that found in observations. It is a significant improvement over the model in SBM15a, although in the reference model the envelope profile in the forbidden emission region is somewhat too steep.

The envelope of the reference model displays bumps wherever the envelope is touched by one of the lines that fan out from the centre. Each line is the projection of a bar-driven spiral arm, as can be seen comparing the upper and lower right-hand panels in Fig. 5. The stronger a spiral arm is, the larger the bump it creates on the envelope.

The black dots in the upper-right panel of Fig. 5 show the points in the Galactic plane that provide the emission that forms the envelope in the  $(l, v)$  plane. Each time a spiral arm in the  $(l, v)$  plane becomes tangent to the envelope, the black dots make a discontinuous jump in the Galactic plane. Particularly strong bumps in the  $(l, v)$  plane and large jumps in the Galactic plane occur at  $l \simeq 18^\circ, v \simeq 150 \text{ km s}^{-1}$ ,  $l \simeq -15^\circ, v \simeq -160 \text{ km s}^{-1}$  and  $l \simeq -20^\circ, v \simeq -140 \text{ km s}^{-1}$ . In Section 3, item (v), we have noted the presence of similar bumps in the observational envelope, including the knee circled in Fig. 3. A faint bump in the reference model at  $l \simeq 9^\circ, v \simeq 210 \text{ km s}^{-1}$  is close to the right position, but is much less strong than the observed knee. We will see below that it can be made stronger by varying the quadrupole. Another bump is present in the observations where the 3kpc arm touches the envelope at  $|l| \simeq -18^\circ, v = -150 \text{ km s}^{-1}$ . This is quite similar to the one present in the reference model at  $l \simeq -20^\circ, v \simeq -140 \text{ km s}^{-1}$ .

In the SBM15a model, bumps were present but were weaker than observed because the spiral arms were barely discernible in the  $(l, v)$  plane. The reference model is a significant improvement, but its knees need to be strengthened and the positions of its bumps tweaked.

Some of the “arms” in the observed  $(l, v)$  plots can be identified with features in the reference  $(l, v)$  plot (Fig. 5). For example, the 3kpc arm and its far-side counterparts are similar to the outermost red arm and its counterpart on the other side, the outermost blue arm. The connecting arm is well traced by part of the innermost green arm, and the arm at  $135 \text{ km s}^{-1}$  is similar to its outer neighbour. Not all arms of the reference model have a counterpart in the observations, but it appears as if all the principal features that contain *arm* in their name have a counterpart in the reference model.

The shocks, traced by the red and blue lines that just touch the  $x_2$  disc in the top right panel of Fig. 5, are very narrow in the Galactic plane, but when projected to the  $(l, v)$  plane show quite a spread in longitude. This suggests that all the vertical features identified in Figure 3 are different portions of the two shocks. In the Galaxy the distribution of gas is not as smooth as in our models, and gas can be more concentrated along regions that, when projected, produce different vertical features. According to the picture proposed by SBM15a, the shock lanes should also form two sides of the CO parallelogram, and the projection of the  $x_2$  disc should match the region of CS emission. The reference model meets this expectation in that both the size of the  $x_2$  disc and the position of the shock lanes in the  $(l, v)$  plane are right. The shocks are not as prominent in the reference  $(l, v)$  plane as in the observed one, probably because the

**Table 1.** Parameters for the reference model described in detail in Sec. 4.

model	$A$	$r_q$ [kpc]	$\Omega_p$ [km s <sup>-1</sup> kpc <sup>-1</sup> ]	$c_s$ [km s <sup>-1</sup> ]	$dx$ [kpc]
Reference	0.6	1.5	40	10	20

model does not include conversion in shocks of gas to molecular form.

The molecular ring, schematically shown in Fig. 3, is well reproduced by our reference model, which becomes darker along a similar diagonal band in the  $(l, v)$  plane. The darkness of the molecular ring in the  $(l, v)$  plane is largely a consequence of velocity crowding: extended areas of material outside the outermost spiral arms in the top left panel in Fig. 5 project to similar values of  $(l, v)$  and hence produce bright intensities in the  $(l, v)$  plane. This is an improvement over the model of SBM15a, which generates an  $(l, v)$  diagram in which the dark band runs too steeply because the gas that generates it is too centrally concentrated, so it projects to low longitudes and high velocities.

We have seen that the reference model, qualitatively, manifests most of the observational signatures of the bar. The next step is to make the correspondence between the model and observed  $(l, v)$  plots quantitatively satisfying. This proves to be a challenging task because changing the model's physical parameters often improves the fit of one feature to the detriment of another. In the next section we study the dependencies of features on parameters that define the bar ( $A, r_q, \Omega_p$ ).

## 5 EFFECTS OF VARYING THE QUADRUPOLE

First we investigate changes to the potential's quadrupole, which is characterised by three parameters: the strength  $A$ , the scale length  $r_q$  and the pattern speed  $\Omega_p$ . The values of these parameters that we have explored are shown in Table 2.

Figs. 6 and 8 show the gas density for different values of quadrupole strength  $A$  and length  $r_q$  and for values of the pattern speed  $\Omega_p = 40 \text{ km s}^{-1} \text{ kpc}^{-1}$  and  $\Omega_p = 60 \text{ km s}^{-1} \text{ kpc}^{-1}$ , respectively. Figs. 7 and 9 show the projections of the same snapshots to the  $(l, v)$  plane, assuming bar angle  $\phi = 20^\circ$ . All snapshots are taken at  $t = 1.25 \text{ Gyr}$ , when all simulations have reached an approximate steady state (apart from any unsteadiness caused by the *wiggle* instability). The reference model has  $\Omega_p = 40 \text{ km s}^{-1} \text{ kpc}^{-1}$  and in Figs. 6 and 7 lies in the panel marked with  $\{A = 0.6, r_q = 1.5\}$ . In order to contain the length of the main text of the paper, we have relegated the results obtained for other values of the pattern speed to Appendix B.

The pattern speed controls the position of the resonances: increasing the pattern speed pushes all the resonances inwards. This is reflected in the morphology of gas flow; many characteristics of the gas flow roughly scale with the locations of the resonances (e.g. SBM15a). For example, comparing Fig. 6 with Fig. 8 demonstrates that increasing the pattern speed pushes spiral arms and the shocks inwards. Table 3 lists the position of the resonances for the explored values of the pattern speed.

From Figs. 6 and 8 we see that the morphology of the arms, the size of the  $x_2$  disc, and the transition point where shocks are formed also depend on both  $A$  and  $r_q$ . Consider the model in the top left panel of Fig. 6,  $\{A = 0.2, r_q = 1\}$ . This model is rather flat and featureless, and this is also reflected in the  $(l, v)$  projection (top left panel of Fig. 7), which does not show anything resembling

**Table 2.** Values of parameters explored in our study.

$A$	$r_q$ [kpc]	$\Omega_p$ [km s <sup>-1</sup> kpc <sup>-1</sup> ]
{0.2, 0.4, 0.6, 0.8}	{1.0, 1.5, 2.0}	{20, 30, 40, 50, 60, 70}

the internal features discussed in Section 3. The model lacks high-velocity peaks, and its  $x_2$  disc is too big to coincide with observed CS emission. It is, however, likely that higher velocity peaks and a smaller  $x_2$  disc would be produced by an increase in sound speed or in resolution (SBM2015a).

By moving down the left column of Fig. 6, we increase the bar strength  $A$  at fixed bar length  $r_q = 1 \text{ kpc}$ . The shock region changes causing the  $x_2$  disc to shrink, but the spiral arms remain weak. In the  $(l, v)$  plane (left column of Fig. 7), the envelope of the emission changes significantly in a way similar to what would be obtained by an increase in sound speed or resolution, but features due to spiral arms remain weak and the resulting diagrams are rather featureless compared to that of the reference model (Fig. 5). This happens because spiral arms appear outside the shock region and are weak when the quadrupole is weak there, as it is when  $\Omega_p = 40 \text{ km s}^{-1} \text{ kpc}^{-1}$  and  $r_q = 1 \text{ kpc}$  (Fig. 2). To strengthen the spirals we need a substantial amount of quadrupole in the region where they are present, hence we must either extend the quadrupole by increasing  $r_q$ , or bring the spirals in by increasing  $\Omega_p$ . The efficacy of the first strategy is illustrated by moving horizontally in either Fig. 6 or Fig. 7, while the efficacy of the second strategy can be seen by comparing equivalent panels in Figs. 6 and 8.

The envelope, by contrast, depends on the flow in the vicinity of the shocks, where the quadrupole strength peaks, and is strongly affected by change in  $A$ . When the quadrupole is strong ( $A = \{0.6, 0.8\}$ ) the gas reaches high velocities and a bigger portion of the forbidden velocity region is covered. Hence the extent of emission at forbidden velocities strongly constrains  $A$ , but barely constrains  $r_q$ .

Stellar dynamics teaches us that bars cannot extend beyond the corotation radius (e.g. Sellwood & Wilkinson 1993), and for any given value of  $\Omega_p$  this fact sets an upper limit on  $r_q$ . The models in the right-hand column of Fig. 8 violate this constraint. These are the models in which the spiral arms are so strong that they have become wobble-unstable shocks.

The bumps on the envelope are strictly connected with the strength of the spiral arms, and their positions are regulated by the parameters that characterise the bar (see, for example, the models with  $A = \{0.6, 0.8\}$  in Fig. 7).

One of the motivations of the present study was to improve the model in SBM15a, which has  $\Omega_p = 63 \text{ km s}^{-1} \text{ kpc}^{-1}$  and a quadrupole very similar to that obtained with  $\{A = 0.2, r_q = 1.5\}$  (Fig. 2). Therefore, let us compare the SBM15a model, computed with the same spatial resolution and sound speed, with the panels for  $\{A = 0.2, r_q = 1.5\}$  in Figs. 8 and 9. The two models are very similar in all aspects: the spiral arms, the transition point, and the size of the  $x_2$  disc. One of the problems of SBM15a model was the lack of spiral arms and consequently of internal features in the  $(l, v)$  plane. Fig. 8 shows that increasing the strength of the quadrupole produces internal features. Another problem of the SBM15a model was that it provided insufficient coverage of forbidden velocities. Fig. 9 shows that a changing the quadrupole strength and length do not cure this problem. A decrease in the pattern speed is needed. We will discuss in more detail the relation to observation in the next section.

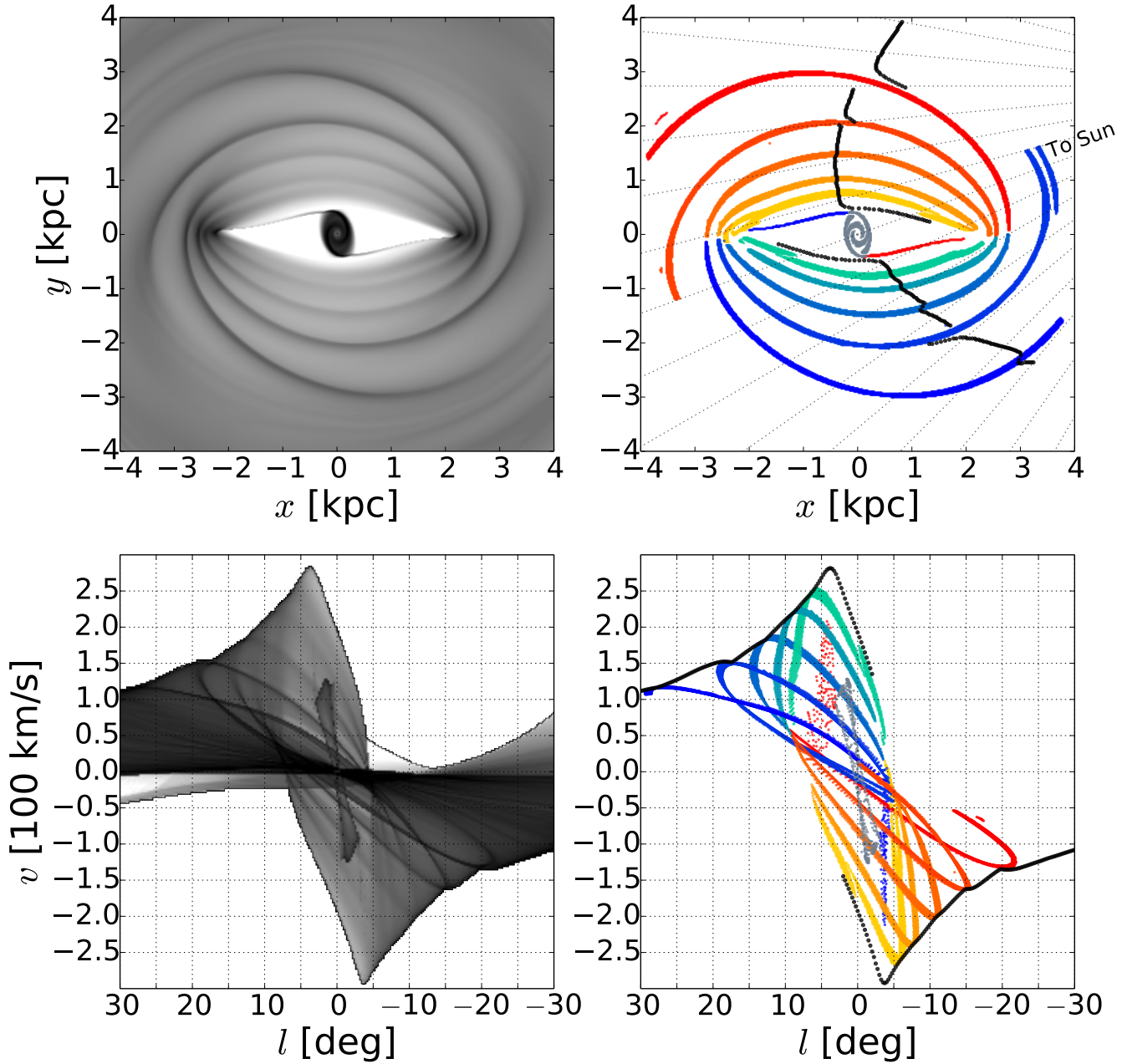


**Figure 5.** The reference model. Top Left: the gas density in the  $xy$  plane. Bottom Left: the projection of the reference model to the  $(l, v)$  plane assuming an angle  $\phi = 20^\circ$ . In the two right panels the same features are shown in  $xy$  and  $(l, v)$  plane using the same colour coding. The black dots trace the points corresponding to the envelope in the  $(l, v)$  plane.

## 6 IMPLICATIONS OF THE OBSERVATIONS

In this section we discuss what our simulations can say about the observations, and in particular about items listed in Section 3.

(i) *Emission at forbidden velocities.* The extent to which emission extends into the forbidden zone of the  $(l, v)$  diagram depends strongly on the pattern speed, and more weakly on the strength and length of the quadrupole. Lower pattern speeds produce more emission in the forbidden zone. When  $\Omega_p \gtrsim 60 \text{ km s}^{-1} \text{ kpc}^{-1}$ , the forbidden emission is insufficiently extended, regardless of the quadrupole's strength and length (Figs. 9 and B8). This statement holds even if we allow the bar angle  $\phi$  to vary. A

good match with observations is obtained at pattern speeds of  $30\text{--}40 \text{ km s}^{-1} \text{ kpc}^{-1}$  (Figs B6 and 7). When the pattern speed is lower,  $\Omega_p \lesssim 20 \text{ km s}^{-1} \text{ kpc}^{-1}$  (Fig. B5), the region is clearly too big for bar angles  $\phi \gtrsim 10^\circ$  that are compatible with photometric data (e.g. Gerhard & Wegg 2014). In light of this finding, it is not surprising that Weiner & Sellwood (1999), who confined their fitting to the envelope, including the forbidden-velocity region, found  $\Omega_p \simeq 42 \text{ km s}^{-1} \text{ kpc}^{-1}$ . Thus, from the forbidden velocities alone, our simulations would suggest a pattern speed in the range  $30\text{--}40 \text{ km s}^{-1} \text{ kpc}^{-1}$ .

(ii) *Velocity peaks.* Discussion of these features is delicate because their structure is sensitive to the spatial resolution of sim-

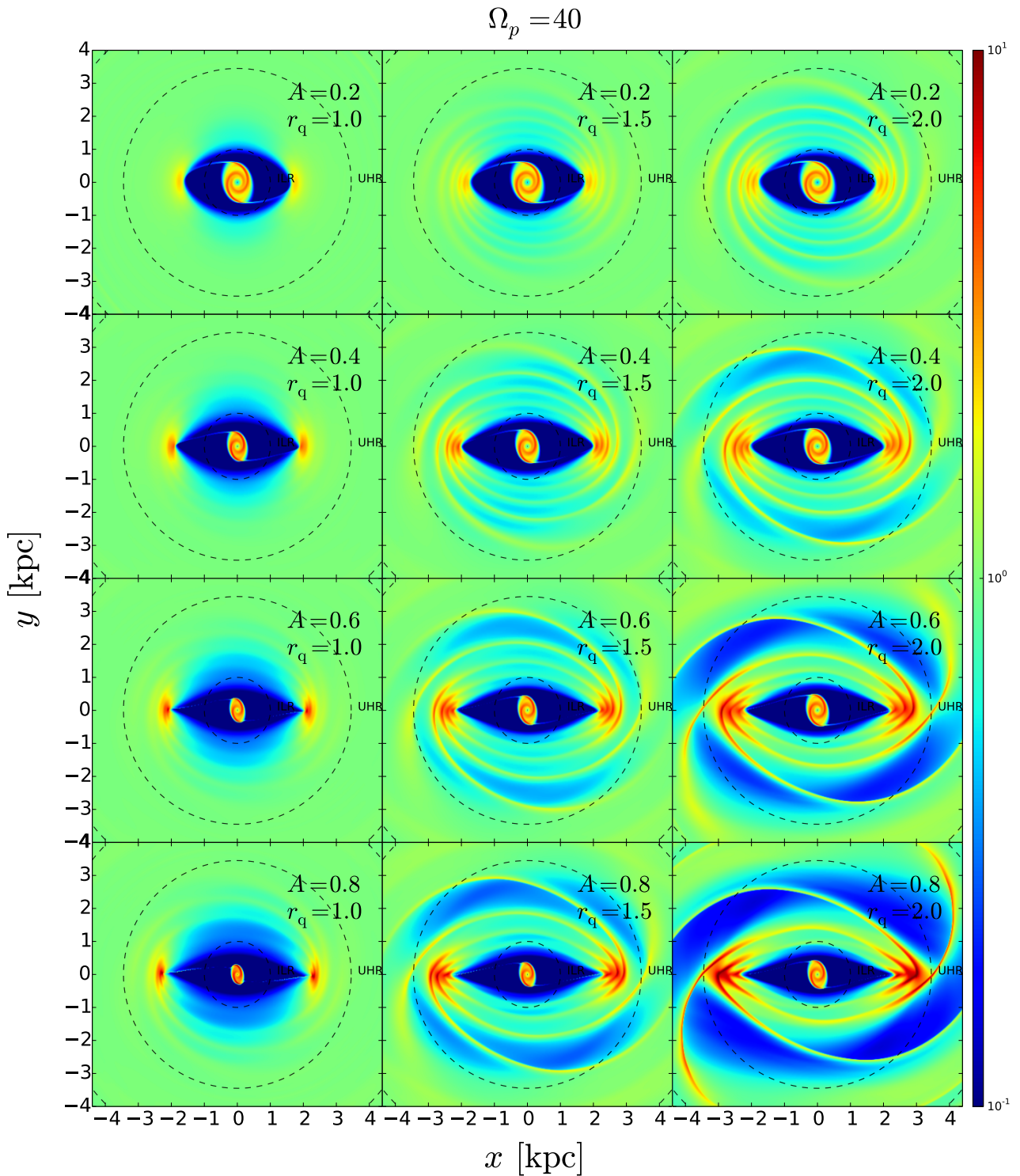


**Figure 6.** The gas surface density in hydro simulations for different values of the quadrupole strength  $A$  and quadrupole length  $r_q$ .  $r_q$  is increasing left to right taking values 1.0, 1.5, 2.0 kpc.  $A$  is decreasing from top to bottom taking values 0.2, 0.4, 0.6, 0.8.  $A$  and  $r_q$  are defined in Eq. (3). All snapshots are for a value of the pattern speed  $\Omega_p = 40 \text{ km s}^{-1} \text{ kpc}^{-1}$ . The major axis of the bar is aligned horizontally, and gas has reached an approximately steady state in the rotating frame and circulates clockwise. All snapshots are taken at  $t = 1.25 \text{ Gyr}$ . The dotted circles mark the positions of the resonances, calculated from the monopole. Since the monopole and  $\Omega_p$  are the same in all panels, the positions of the resonances are identical for all of them. The colorbar is in units of  $M_\odot \text{ pc}^{-2}$



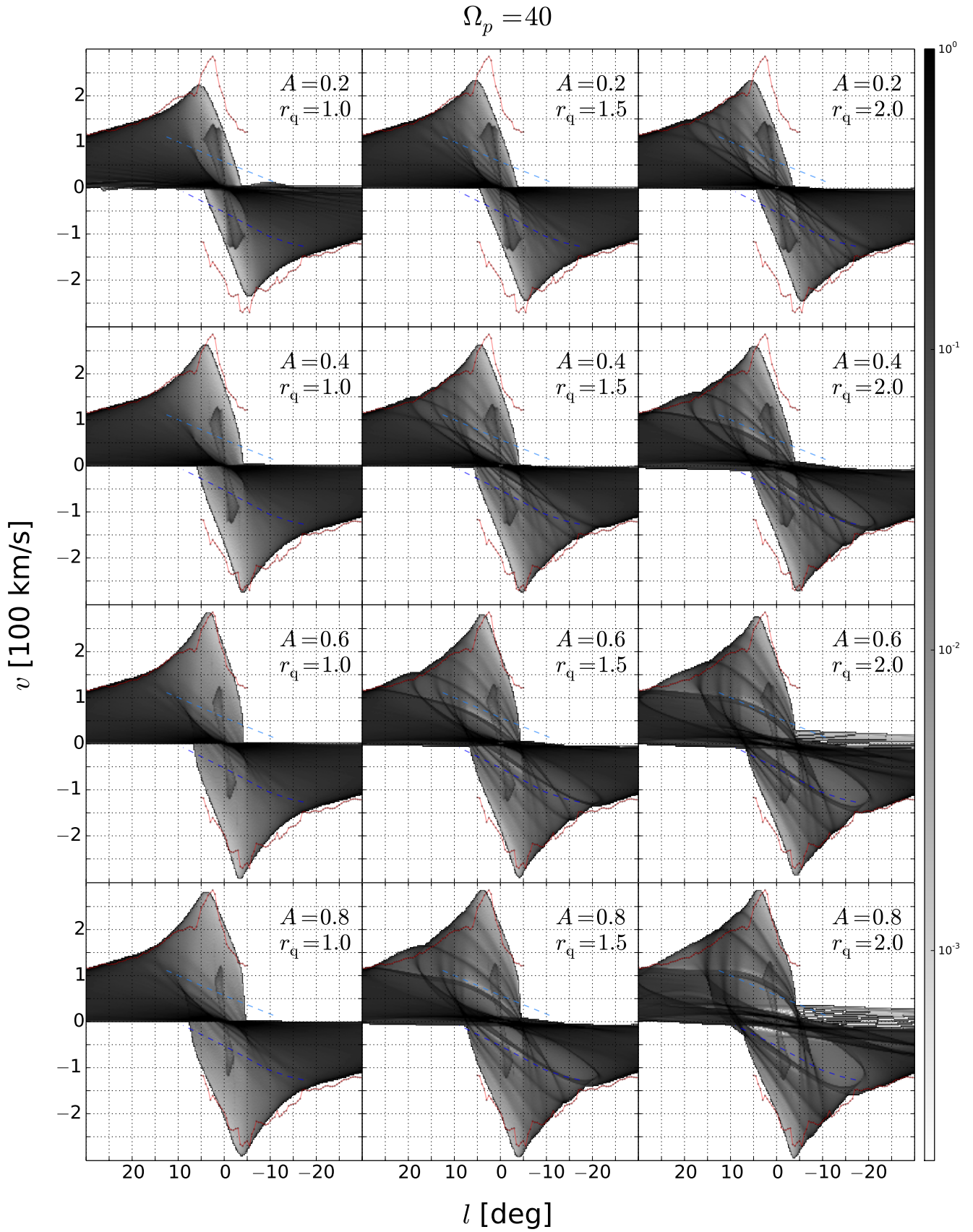


**Figure 7.** The simulations of Fig. 6 projected into the  $(l, v)$  plane. The Sun is assumed to be in a circular orbit with  $v = 220 \text{ km s}^{-1}$  at  $R_0 = 8 \text{ kpc}$ , and the bar major axis makes an angle  $\phi = 20^\circ$  with the Sun-Galactic centre line. The red dots trace the envelope of the observations, while the blue dashed lines indicate the positions of the near and far 3 kpc arms. Since the projections can be scaled freely, the colorbar is in arbitrary units.



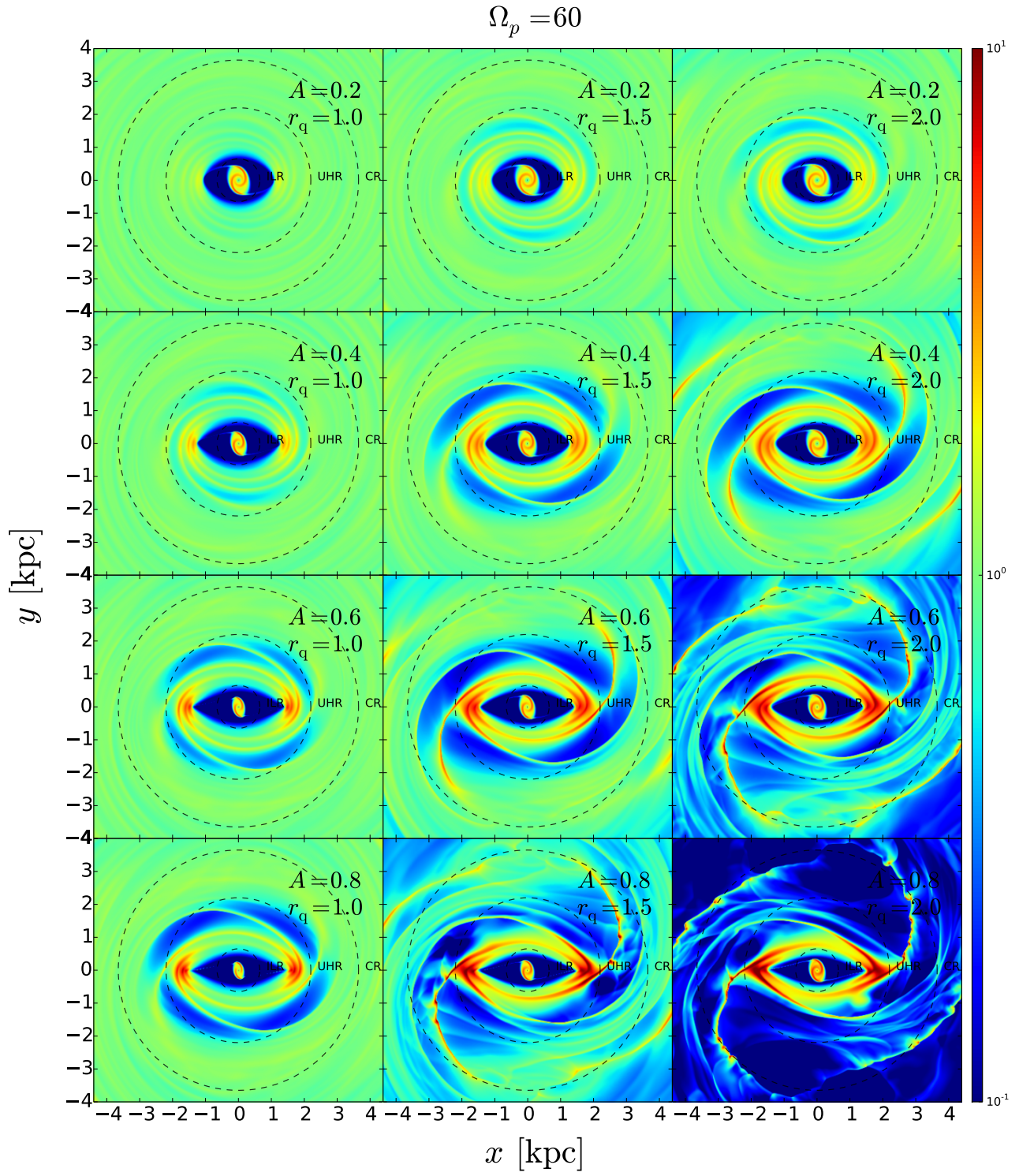


**Figure 8.** Same as Fig. 6 but for a pattern speed  $\Omega_p = 60 \text{ km s}^{-1} \text{ kpc}^{-1}$ .

$$\Omega_p = 60$$

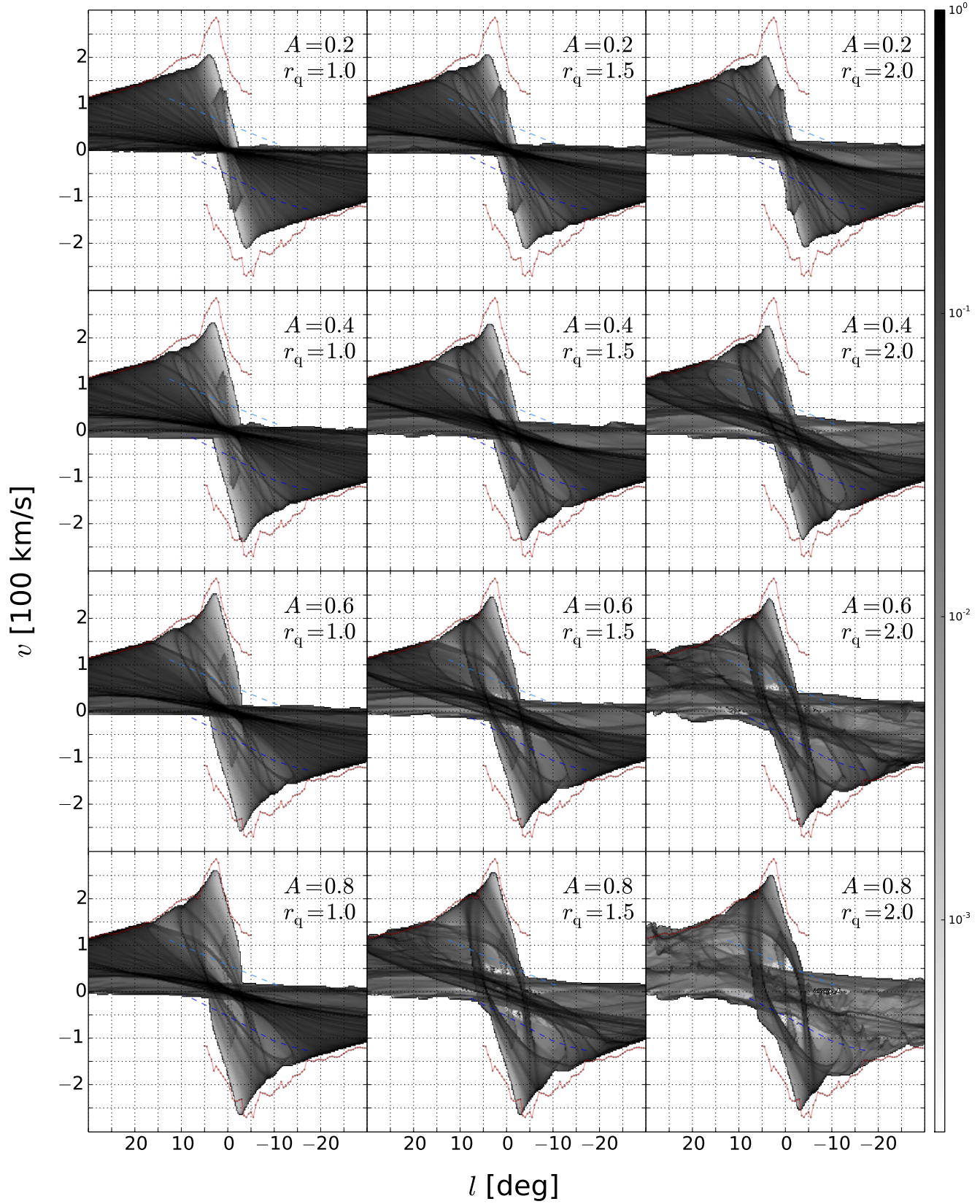


Figure 9. Same as Fig. 7 but referring to Fig. 8.

**Table 3.** Positions of resonances for different values of the pattern speed. ILR = Inner Lindblad Resonance, UHR = Ultra Harmonic Resonance (i.e., 4/1), CR = corotation, OLR = Outer Lindblad Resonance. These are calculated from the monopole, black curve in Fig. 1.

$\Omega_p$ [ $\text{km s}^{-1} \text{kpc}^{-1}$ ]	ILR [kpc]	UHR [kpc]	CR [kpc]	OLR [kpc]
20	2.85	7.35	10.40	14.25
30	1.85	4.75	7.35	10.90
40	1.00	3.45	5.60	8.85
50	0.80	2.70	4.45	7.40
60	0.65	2.20	3.65	6.30
70	0.55	1.85	3.10	5.45

ulations (SBM15a). For example, in models with weak bars (e.g. top row in Fig. 9) the peaks are not reproduced, but the results of SBM15a show that they would be reproduced at higher resolution. The velocity peaks depend very weakly on the bar length (Figs. 7 and 9), and only marginally more strongly on the bar strength  $A$ , especially once we consider the effects of resolution. Increasing the pattern speed shifts the peaks to lower longitudes. For the chosen angle  $\phi = 20^\circ$ , the peak at positive velocity is at the right longitude when the pattern speed is high,  $\Omega_p \simeq 60 \text{ km s}^{-1} \text{ kpc}^{-1}$ , while it is at slightly too high longitudes when the pattern speed is lower. The peak at negative velocity instead is at the right longitude when the pattern speed is low,  $\Omega_p \simeq 40 \text{ km s}^{-1} \text{ kpc}^{-1}$ , and appears at slightly too low longitudes when the pattern speed is higher.

(iii) *Internal features.* Internal features provide some of the tightest constraints on the quadrupole’s length and strength. As discussed in Section 5, a significant quadrupole is needed at  $\sim 3 \text{ kpc}$  to produce the observed arms (e.g. left column in Fig. 7). No model with a short bar,  $r_q = 1$ , produces the requisite quadrupole. Shifting the pattern speed significantly from  $\Omega_p = 40 \text{ km s}^{-1} \text{ kpc}^{-1}$ , in either direction, shifts the region in which spirals can form away from the radial range specified by the data (See Appendix B for details). The 3 kpc arm extends to  $|l| \simeq 20^\circ$ , so a substantial quadrupole is required at the arm’s tangent point,  $R_0 \sin(20^\circ) \simeq 3 \text{ kpc}$ . If the bar is this long, stellar dynamics excludes pattern speeds as high as  $\Omega_p = 60 \text{ km s}^{-1} \text{ kpc}^{-1}$ . Thus, internal features strongly suggest that the bar pattern speed is around  $\Omega_p = 40 \text{ km s}^{-1} \text{ kpc}^{-1}$ . This is perhaps why Rodriguez-Fernandez & Combes (2008), who used the 3 kpc arm as a fitting criterion, favoured a pattern speed in the range  $\Omega_p = 30\text{--}40 \text{ km s}^{-1} \text{ kpc}^{-1}$ . Other models with higher pattern speeds, (Englmaier & Gerhard 1999; Bissantz et al. 2003) reproduce the internal features less well. The molecular ring is also better reproduced when the pattern speed is  $\Omega_p = 40 \text{ km s}^{-1} \text{ kpc}^{-1}$ . These models become darker along the right diagonal band in the  $(l, v)$  plane, similarly to the reference model in Sect. 4. When the pattern speed is higher or lower, this band becomes too much or not enough centrally concentrated respectively.

(iv) *The Envelope.* In the positive-longitude permitted quadrant, ( $l > 0, v > 0$ ), the envelope is well matched by simulations with high pattern speed,  $\Omega_p = 50\text{--}60 \text{ km s}^{-1} \text{ kpc}^{-1}$  (Figs. B7 and 9). When the pattern speed is lower, (e.g., Fig. 7), the predicted envelope is generally higher than the observed one and the descent immediately after the peak towards larger longitudes is too shallow; in other words, the peaks are not sharp enough. In the other permitted quadrant however, ( $l < 0, v < 0$ ), the opposite is true and the envelope is well matched by simulations with low pattern speed,  $\Omega_p = 40 \text{ km s}^{-1} \text{ kpc}^{-1}$ , while at higher pattern speed the models do not reach adequately high velocities and are too steep. Regard-

ing the envelope at forbidden velocities, a better match is obtained at low pattern speeds, as noted in item (i) above. Thus, the envelope is sending mixed message as regards the pattern speed. Perhaps tweaking the monopole and the bar angle  $\phi$  one would obtain a good fit to the envelope in both the permitted quadrants for a low pattern speed. Although the mere presence of the quadrupole dramatically changes the envelope from its form in the axisymmetric case, the envelope’s form is surprisingly insensitive to the quadrupole’s exact length and strength.

(v) *Bumps on the Envelope* The strength and position of the bumps in the envelope where it is touched by a spiral arm are sensitive to the quadrupole parameters  $A$  and  $r_q$ . The bump associated with the near 3 kpc arm is very well reproduced at low pattern speed (Fig. 7) when the bar is long and strong ( $A \gtrsim 0.6, r_q \gtrsim 1.5$ ). The knee is also close to the right position in some of the same models – for example, in the model  $\{A = 0.8, r_q = 2.0\}$ . When the pattern speed is higher (Fig. 9), the knee is also well reproduced in some models but these models don’t fit the 3 kpc arm and its bump. Changing the viewing angle  $\phi$  moves the bumps in longitude without much change to their structures.

Overall the observations are best fitted when the pattern speed is  $\Omega_p \simeq 40 \text{ km s}^{-1} \text{ kpc}^{-1}$ . Only one aspect is better explained with a higher pattern speed of  $\Omega_p = 60 \text{ km s}^{-1} \text{ kpc}^{-1}$ : the sharpness of the positive longitude velocity peak and the associated portion of the envelope in the positive-velocity permitted quadrant. It seems likely, although it is not guaranteed, that these shortcomings can be resolved by tweaking the monopole component of the potential, as well as the other parameters that define the bar and the gas flow. Moreover, the internal features strongly suggest that the bar is longer than it could be with a high pattern speed: their extension to large longitudes requires a long quadrupole that is difficult to reconcile with the constraints from stellar dynamics. The presence of a long bar has also been confirmed by photometric evidence by the recent work of Wegg & Gerhard (2013) and Wegg et al. (2015). Hence, we favour a pattern speed  $\Omega_p \simeq 40 \text{ km s}^{-1} \text{ kpc}^{-1}$ , in agreement with the determinations of Fux (1999), Weiner & Sellwood (1999) and Rodriguez-Fernandez & Combes (2008) and slightly higher than the value of  $25\text{--}30 \text{ km s}^{-1} \text{ kpc}^{-1}$  determined by Portail et al. (2015).

We should also mention that many other parameters influence fits to the observations. The bar angle  $\phi$  and the sound speed are particularly relevant. Also, simulations are known to be affected by resolution effects (SBM15a). We have neglected these parameters in this paper in part because they have been studied in other papers (e.g. Englmaier & Gerhard 1997; Patsis & Athanassoula 2000, SBM15a). Had we included them in our discussion, the parameter space to explore would have been intractably large. As an addition, we report that we have repeated our simulations with a higher sound speed of  $c_s = 20 \text{ km s}^{-1}$  and we have found increasing the sound speed can reduce the number of spiral arms but does not materially affect the principal conclusions of this paper.

Another question of interest regards the importance of self-gravity. To test this, we have carried a small number of simulations in the SBM15a potential taking into account the gravitational potential generated by the gas, in addition to that of the stars that is assumed to be externally imposed as before. We found that self-gravity of the gas is generally negligible when the gas density has realistic values and should be taken into account as a refinement only after signatures of the bar described above have been better constrained. These simulations only refers to the large-scale effects of self-gravity; on smaller scales not studied in this paper it

is known that self-gravity is important in maintaining the structure of individual ISM clouds. An open issue, however, is how much the gas is affected by the spiral response of the stars to the bar perturbation.

## 7 CONCLUSION

The model presented in Sormani et al. (2015a) had two major shortcomings. One was the lack of internal features, that could reproduce, for example, the 3kpc arm, and the other was the lack of emission at forbidden velocities. We have run many simulations, varying systematically the quadrupole component of the bar potential, and we have found that both these shortcomings can be cured by adjusting the pattern speed and the quadrupole length and strength. However, we have failed to find a set of parameters that reproduces all the important observational features simultaneously. Good fits to individual features can be often obtained to the detriment of other features.

Our exploration of the quadrupole parameter space suggests that the pattern speed of the bar is around  $\Omega_p = 40 \text{ km s}^{-1} \text{ kpc}^{-1}$  and that the bar exponential scale length as defined in equation (3) must be at least  $r_q = 1.5 \text{ kpc}$ , while  $r_q = 1 \text{ kpc}$  is too short. The bar strength, defined in the same equation, must be at least  $A = 0.4$ . In our study we haven't explored all the parameters that are important in fitting the Milky Way: in particular, we have kept the angle between the major axis of the bar and the Sun-Galactic centre line constant at the value  $\phi = 20^\circ$ . Other parameters characterising the model, such as the potential's monopole component, and the sound speed, play an important role in determining the gas flow. The resulting parameter space is too big to be tractable with by-eye fitting methods. To obtain a model that can reproduce all the important features simultaneously, automatic quantitative methods to search in parameter space such as that described in Sormani & Magorrian (2015) are promising and should be explored.

## ACKNOWLEDGEMENTS

MCS acknowledges the support of the Clarendon Scholarship Fund. JB and JM were supported by Science and Technology Facilities Council by grants R22138/GA001 and ST/K00106X/1. JM acknowledges support from the "Research in Paris" programme of Ville de Paris. The research leading to these results has received funding from the European Research Council under the European Union's Seventh Framework Programme (FP7/2007-2013) / ERC grant agreement no. 321067.

## REFERENCES

Athanassoula E., 1992, MNRAS, 259, 345  
 Baba J., Saitoh T. R., Wada K., 2010, pasj, 62, 1413  
 Bally J., Stark A. A., Wilson R. W., Henkel C., 1988, ApJ, 324, 223  
 Bania T. M., 1977, ApJ, 216, 381  
 Binney J., Gerhard O., Spergel D., 1997, MNRAS, 288, 365  
 Binney J., Gerhard O. E., Stark A. A., Bally J., Uchida K. I., 1991, MNRAS, 252, 210  
 Binney J., Merrifield M., 1998, Galactic Astronomy. Princeton University Press  
 Bissantz N., Englmaier P., Gerhard O., 2003, MNRAS, 340, 949

Burton W. B., Elmegreen B. G., Genzel R., eds., 1992, The galactic interstellar medium  
 Cohen R. J., 1975, MNRAS, 171, 659  
 Dame T. M., Hartmann D., Thaddeus P., 2001, ApJ, 547, 792  
 Dame T. M., Thaddeus P., 2008, ApJ, 683, L143  
 Dwek E. et al., 1995, ApJ, 445, 716  
 Englmaier P., Gerhard O., 1997, MNRAS, 287, 57  
 Englmaier P., Gerhard O., 1999, MNRAS, 304, 512  
 Ferrière K. M., 2001, Reviews of Modern Physics, 73, 1031  
 Fux R., 1999, A&A, 345, 787  
 Fux R., 2004, in Astrophysics and Space Science Library, Vol. 315, How Does the Galaxy Work?, Alfaro E. J., Pérez E., Franco J., eds., p. 213  
 Gerhard O., Wegg C., 2014, ArXiv e-prints  
 Jenkins A., Binney J., 1994, MNRAS, 270, 703  
 Kalberla P. M. W., Burton W. B., Hartmann D., Arnal E. M., Bajaja E., Morras R., Pöppel W. G. L., 2005, A&A, 440, 775  
 Kim W.-T., Kim Y., Kim J.-G., 2014, ApJ, 789, 68  
 Lee C. W., Lee H. M., Ann H. B., Kwon K. H., 1999, ApJ, 513, 242  
 Liszt H. S., Burton W. B., 1980, ApJ, 236, 779  
 Mulder W. A., Liem B. T., 1986, A&A, 157, 148  
 Patsis P. A., Athanassoula E., 2000, A&A, 358, 45  
 Pettitt A. R., Dobbs C. L., Acreman D. M., Bate M. R., 2015, MNRAS, 449, 3911  
 Pettitt A. R., Dobbs C. L., Acreman D. M., Price D. J., 2014, MNRAS, 444, 919  
 Portail M., Wegg C., Gerhard O., Martínez-Valpuesta I., 2015, MNRAS, 448, 713  
 Rodríguez-Fernández N. J., Combes F., 2008, A&A, 489, 115  
 Rougoor G. W., 1964, Bulletin of the Astronomical Institutes of the Netherlands, 17, 381  
 Sale S. E., Magorrian J., 2014, MNRAS, 445, 256  
 Sellwood J. A., Wilkinson A., 1993, Reports on Progress in Physics, 56, 173  
 Sormani M. C., Binney J., Magorrian J., 2015a, MNRAS, 449, 2421  
 Sormani M. C., Binney J., Magorrian J., 2015b, MNRAS, 451, 3437  
 Sormani M. C., Magorrian J., 2015, MNRAS, 446, 4186  
 Stanek K. Z., Mateo M., Udalski A., Szymanski M., Kaluzny J., Kubiak M., 1994, ApJletters, 429, L73  
 van Albada G. D., van Leer B., Roberts, Jr. W. W., 1982, A&A, 108, 76  
 van der Kruit P. C., 1970, A&A, 4, 462  
 Wada K., Koda J., 2004, MNRAS, 349, 270  
 Wegg C., Gerhard O., 2013, MNRAS, 435, 1874  
 Wegg C., Gerhard O., Portail M., 2015, ArXiv e-prints  
 Weiner B. J., Sellwood J. A., 1999, ApJ, 524, 112

## APPENDIX A: LONGITUDE-VELOCITY DIAGRAMS VARIATION BY LATITUDE

## APPENDIX B: RESULTS OF THE SIMULATION FOR OTHER VALUES OF THE PATTERN SPEED

In this appendix we show the results for other values of the pattern speed as a reference.



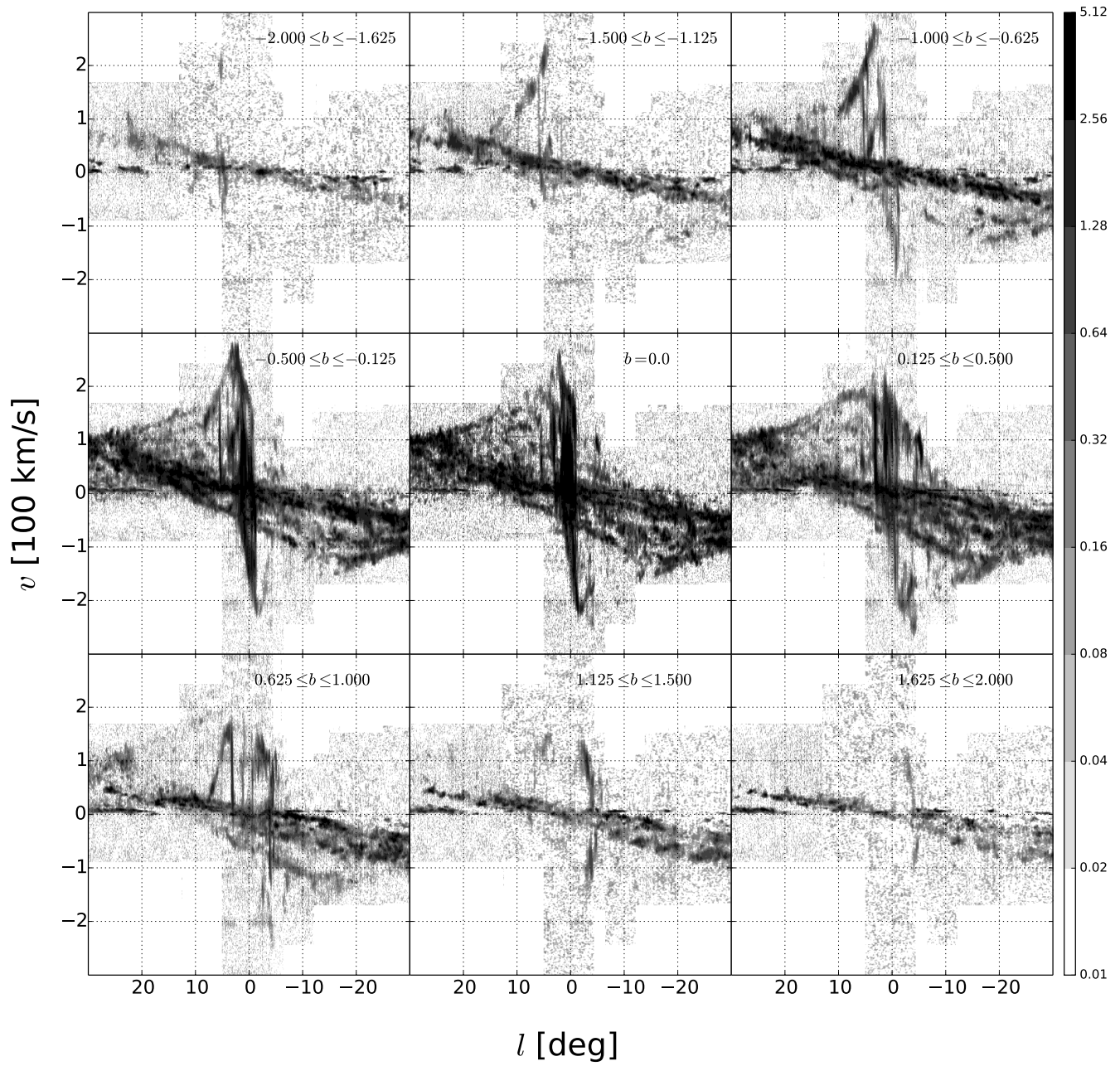
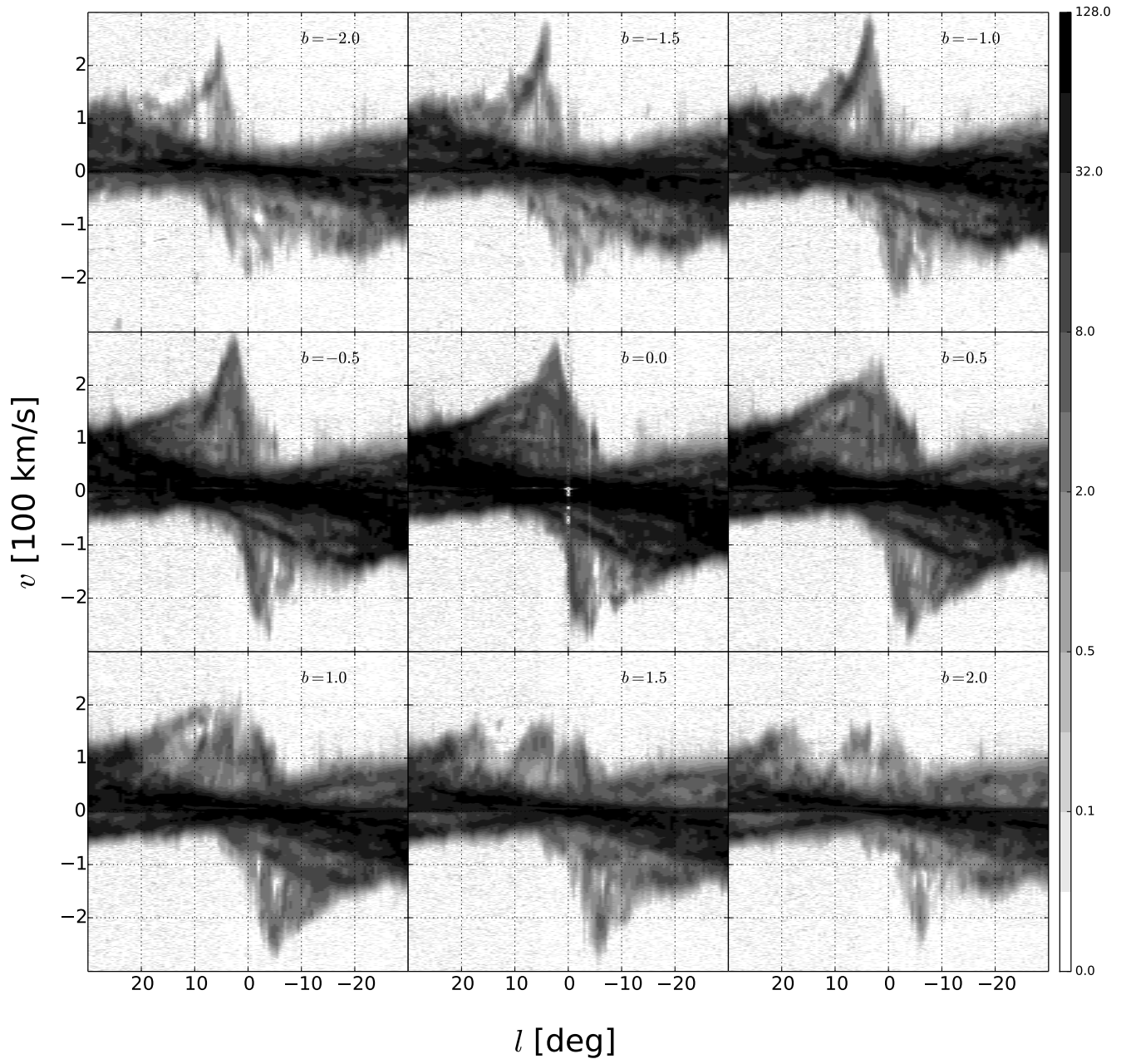
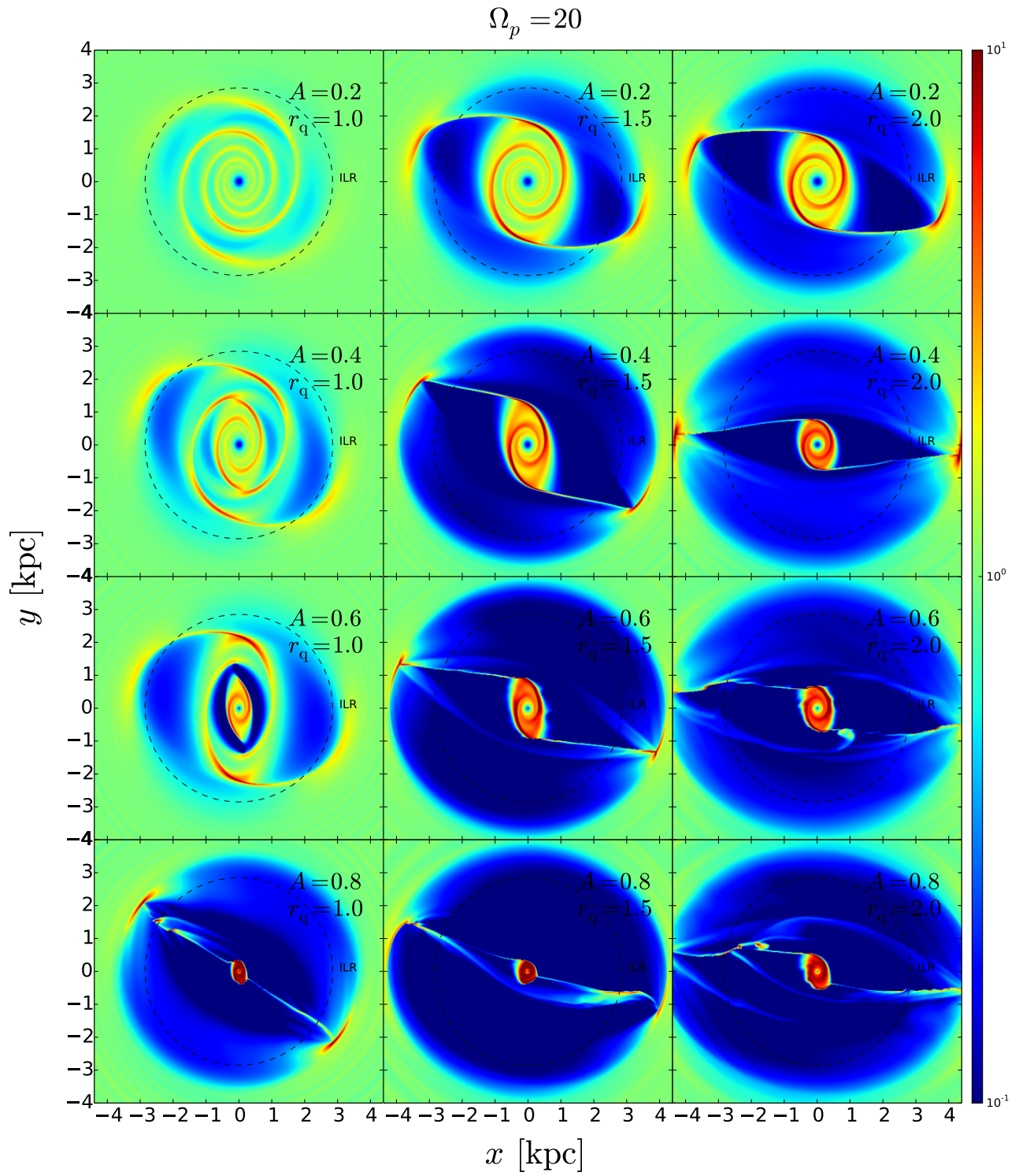


Figure A1. Slices at different latitude  $b$  of the same CO data shown Fig. 4.





**Figure A2.** Slices at different latitude  $b$  of the same HI data shown in Fig. 4.



**Figure B1.** Same as Fig. 6 but for a pattern speed  $\Omega_p = 20 \text{ km s}^{-1} \text{ kpc}^{-1}$ .

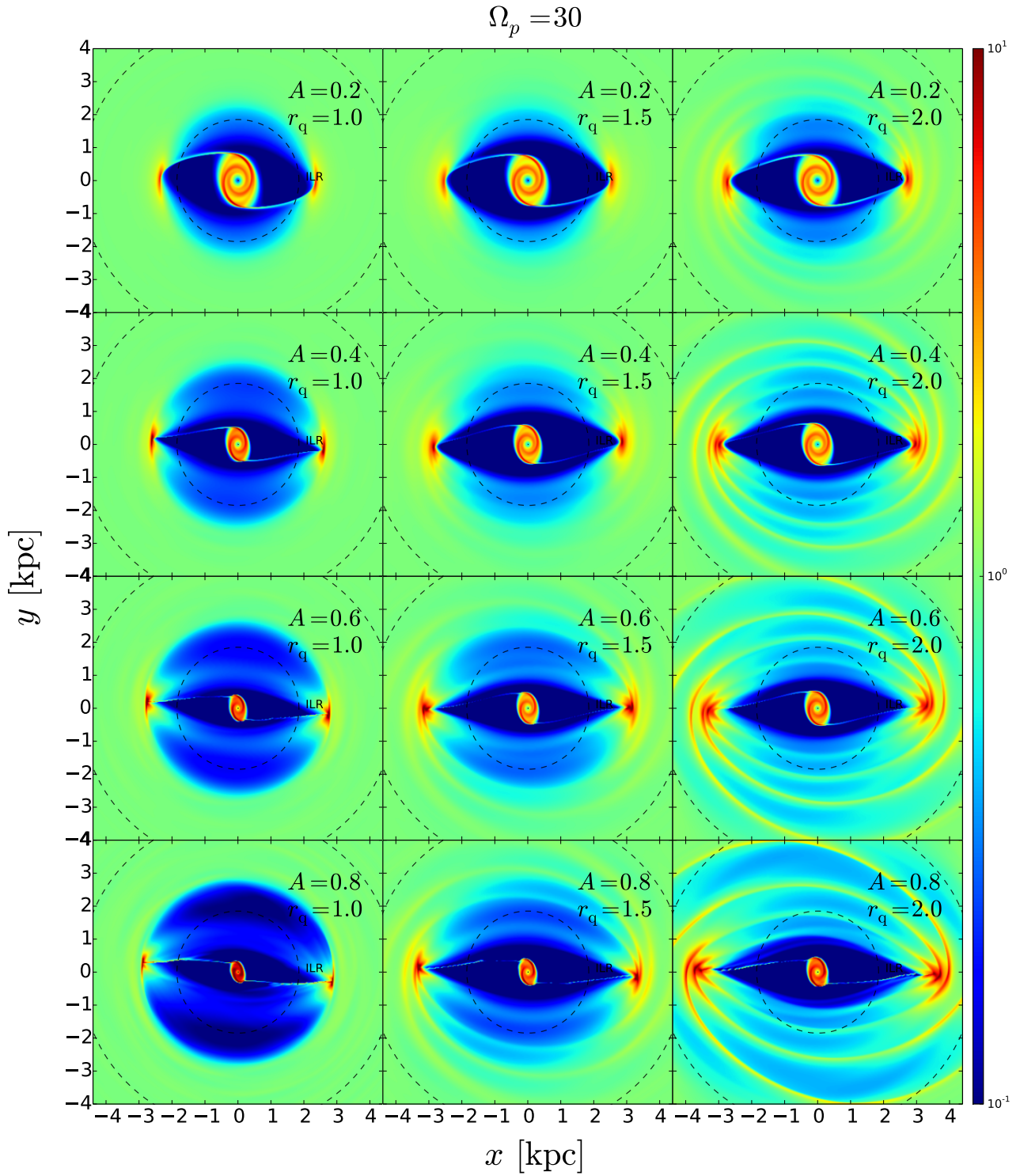


**Figure B2.** Same as Fig. 6 but for a pattern speed  $\Omega_p = 30 \text{ km s}^{-1} \text{ kpc}^{-1}$ .



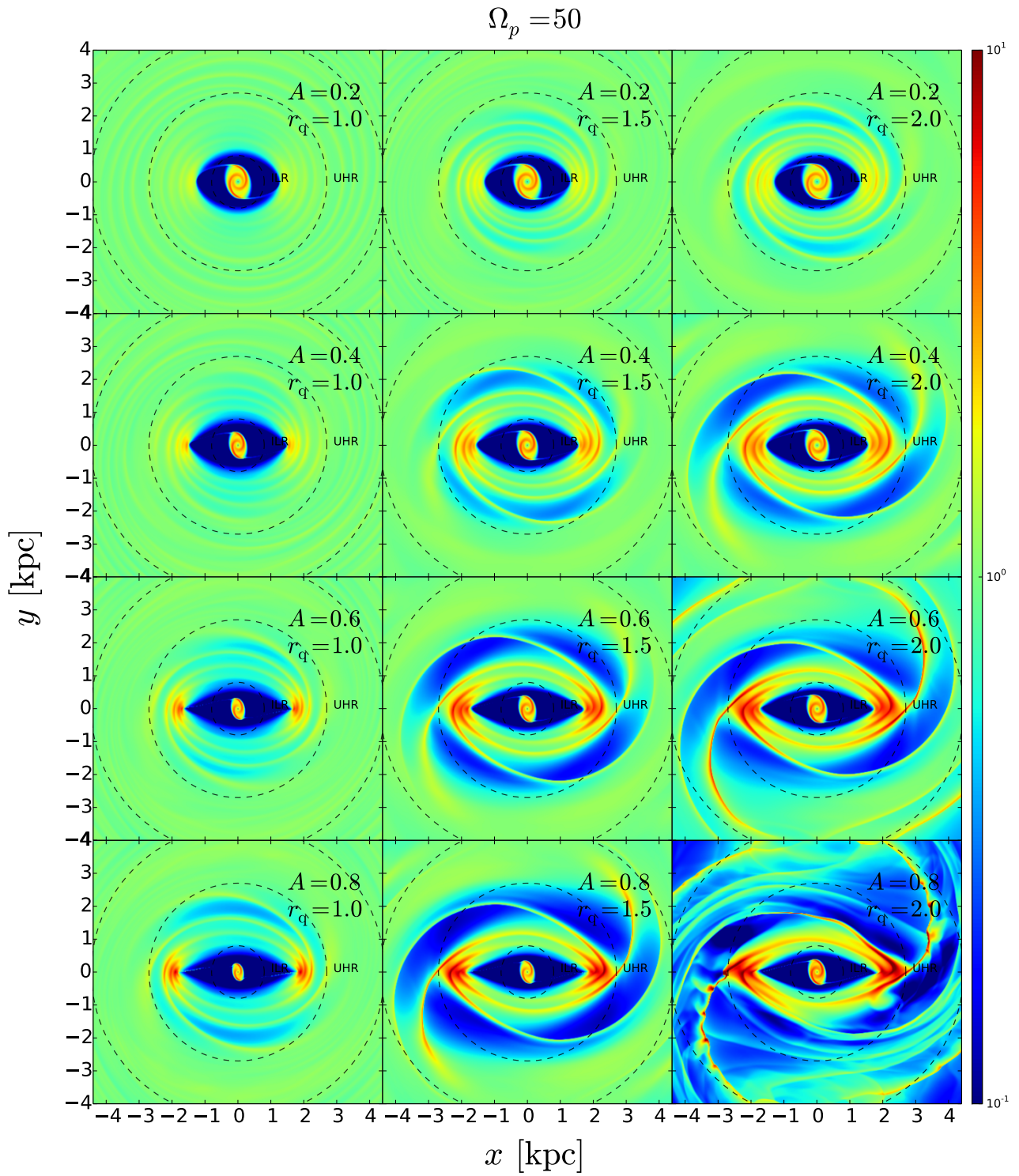


**Figure B3.** Same as Fig. 6 but for a pattern speed  $\Omega_p = 50 \text{ km s}^{-1} \text{ kpc}^{-1}$ .

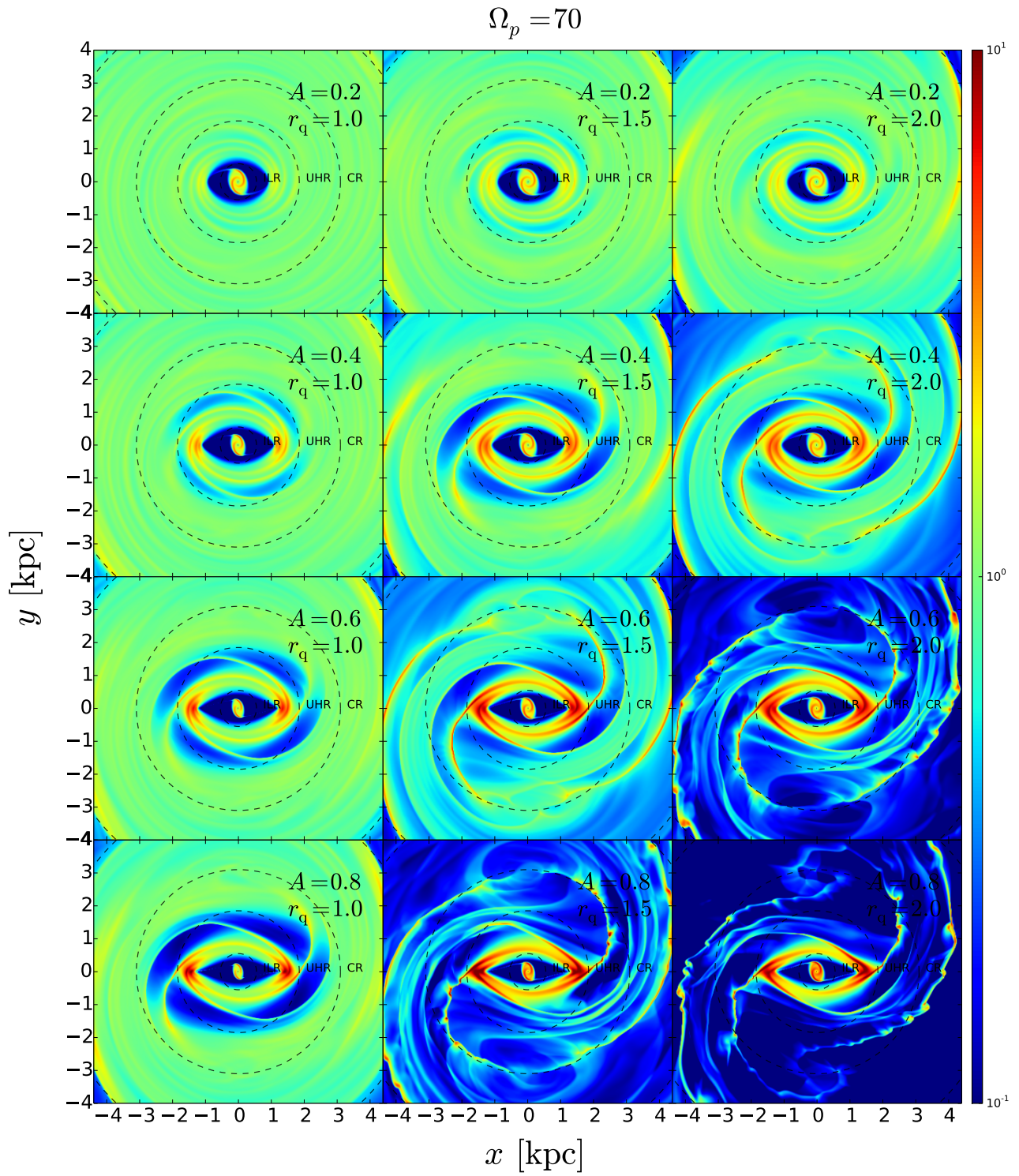


**Figure B4.** Same as Fig. 6 but for a pattern speed  $\Omega_p = 70 \text{ km s}^{-1} \text{ kpc}^{-1}$ .



$$\Omega_p = 20$$

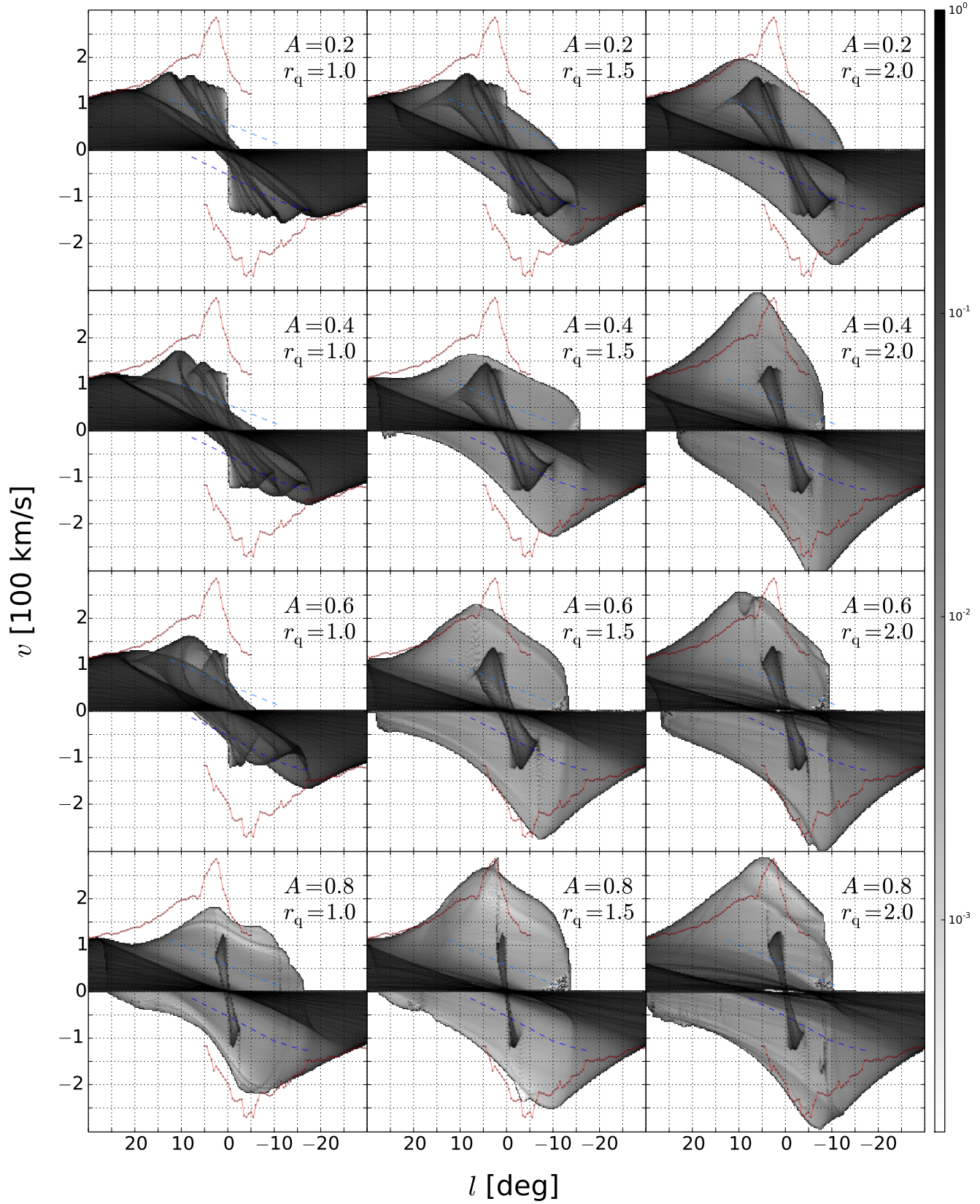


Figure B5. Same as Fig. 7 but referring to Fig. B1.

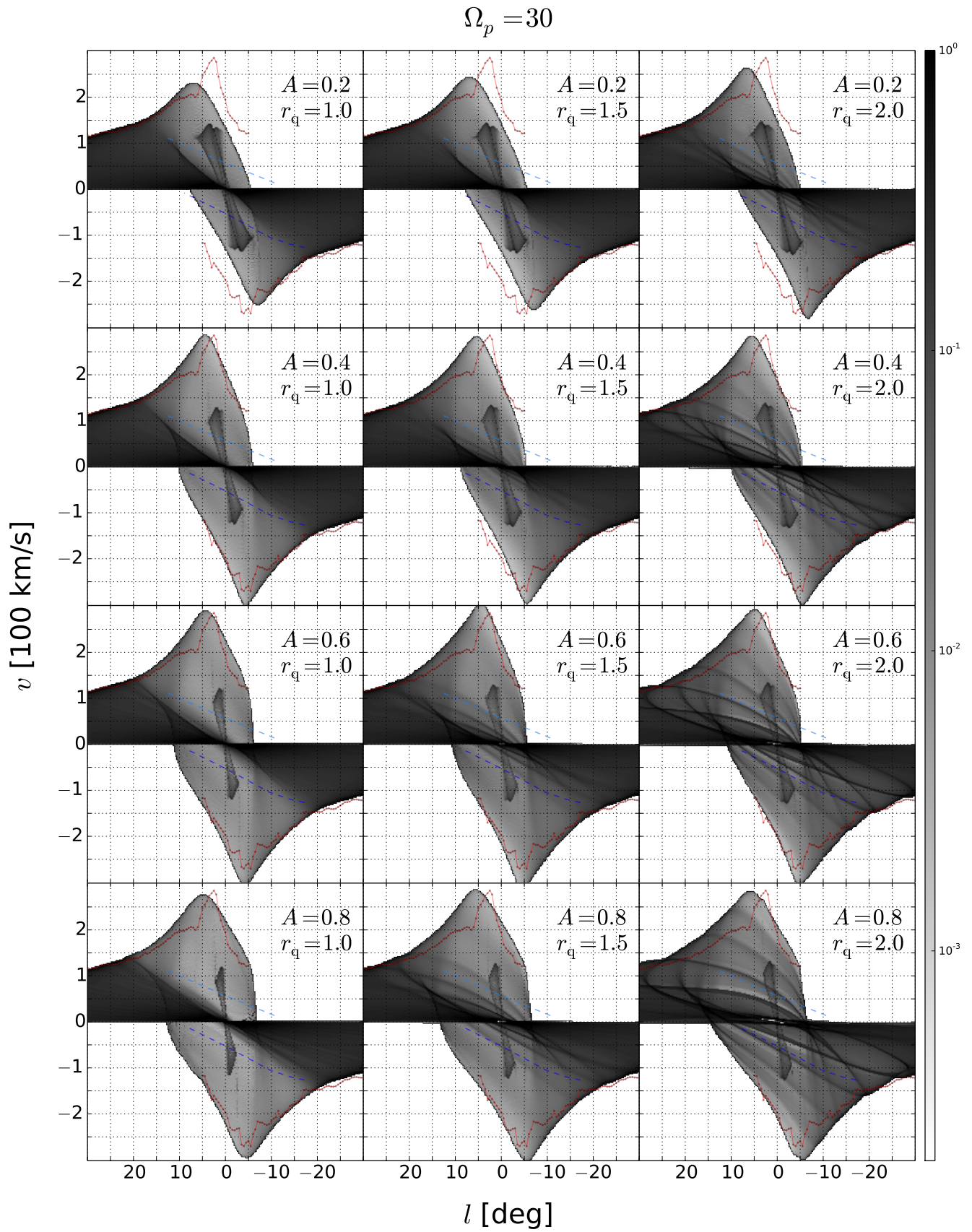


Figure B6. Same as Fig. 7 but referring to Fig. B2.

$$\Omega_p = 50$$

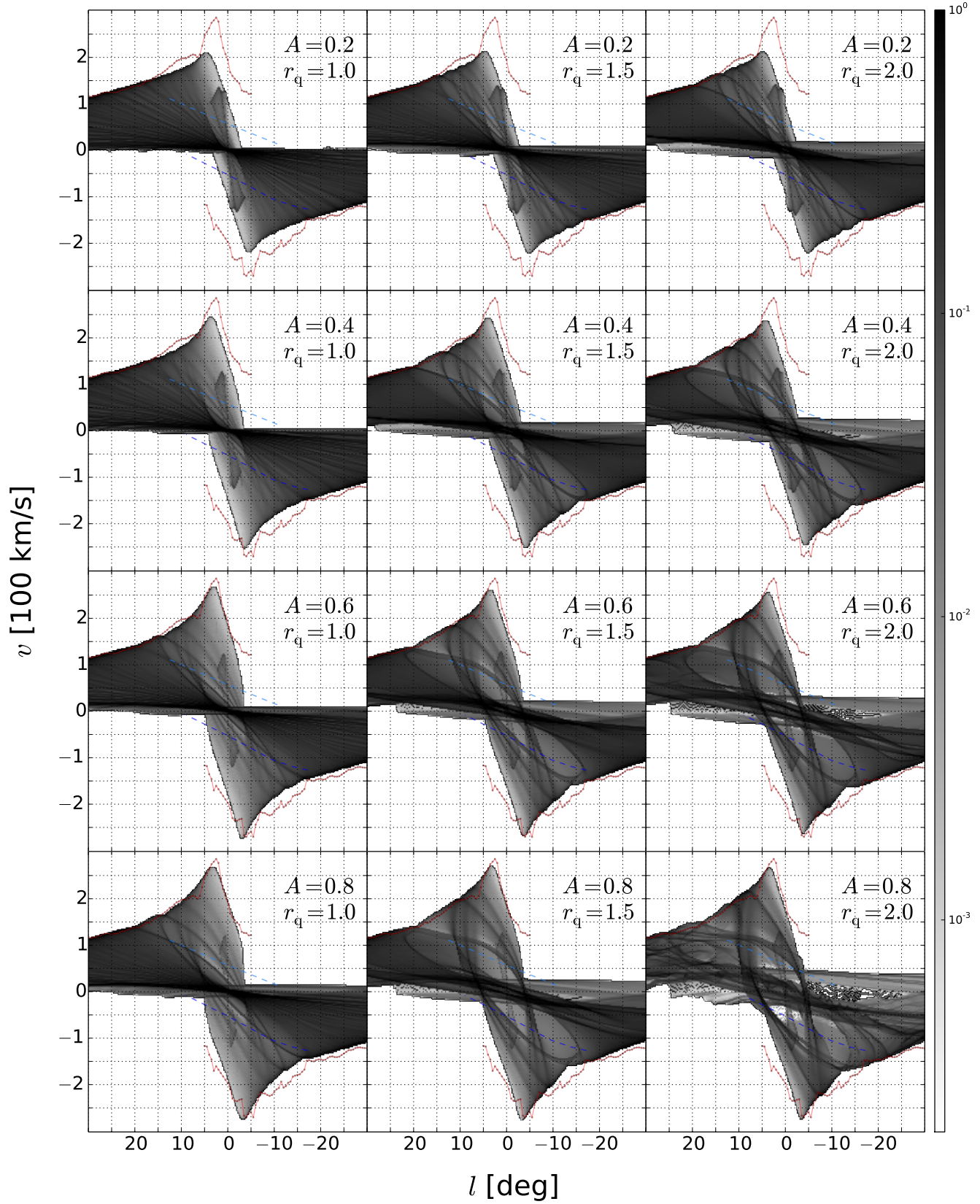


Figure B7. Same as Fig. 7 but referring to Fig. B3.



$$\Omega_p = 70$$

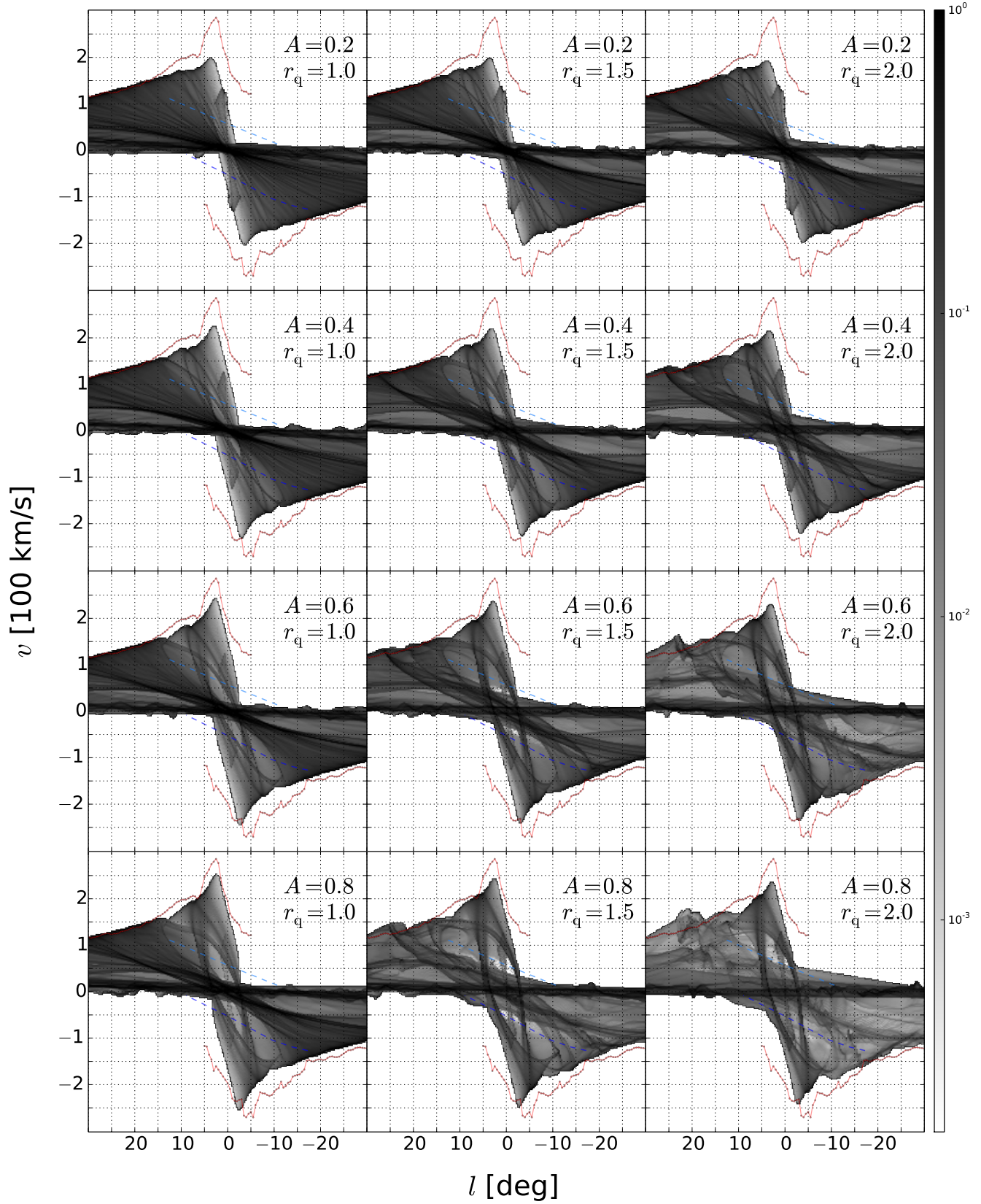


Figure B8. Same as Fig. 7 but referring to Fig. B3.